A Search for Neutral, Heavy Particles Decaying to a Neutrino and a Single Photon at the SPS Wide-Band Neutrino Beam

by

David Michael Steele

A dissertation submitted to the
The Johns Hopkins University
in conformity with the requirements for the degree of
Doctor of Philosophy

Work supported by the National Science Foundation
through grant NSF PHY-9526278 under the direction
of Barry Blumenfeld

Abstract

A search is performed for single, isolated photons from $\mathcal{X}^0$ decay, where $\mathcal{X}^0$ represents either a neutrino excited state or an unknown, neutral, massive particle produced in a rare π^+ decay along the neutrino beam line as hypothesized by the KARMEN Collaboration[1] as a possible solution to their anomalous time spectra for $\pi^+ \to \mu^+ + \nu_\mu$. The analysis is performed using data from the NOMAD (WA96) experiment in the wide-band ν_μ beam using the SPS accelerator situated at the European Center for Nuclear Research near Geneva, Switzerland. Out of a flux of ν_μ resulting from 6.13×10^{18} protons on target, seven events pass all cuts. The relative abundance of these events is entirely consistent with those expected from neutrino interactions in the detector. Upper limits are set at 90% confidence level for the production rate of this particle as a function of its lifetime.

Acknowledgements

A graduate student in neutrino physics would have a hard time finding a better advisor than Barry Blumenfeld. He has given me an immense amount of guidance for this dissertation and taught me a great deal about physics in general. At the same time, he does not "micro-manage" his students, but encourages them to explore things on their own. For this dissertation, he has provided direction for the analysis and has made substantial contributions to the Monte Carlo chapter. I sincerely thank him for all he has done for me.

I would like to thank everyone in the NOMAD collaboration, especially François Vannucci for doing so much to organize and motivate the collaboration from its outset. In addition, a large number of people have been particularly helpful to me. Achim Geiser has provided me with ideas and suggestions about all types of physics as well as acting as a "sounding board" for many of my ideas. Ian Bird, Patrick Nédélec, Chiara Roda, and Alan Grant provided me with more than everything needed to process the data. Burkhard Schmidt helped with numerous discussions involving the trigger electronics

and the data-acquisition. Emmanuel Tsesmelis provided me with a plethora of information regarding the neutrino beam and its simulation. Thomas Weiße did me several great services by his work on the 1995 ECal data and the corresponding event simulation. Thanks to Peter Hurst and Tom Dignan for their help with the hadronic calorimeter. Tom should also be thanked for the occasional, much-needed, comic relief. Luigi DiLella and Leslie Camilleri have always supported my work in the various parts of NOMAD, for which I am very grateful.

I would like to thank the INFN and the entire electromagnetic calorimeter group for building and supporting such a nice piece of hardware; similarly, the Lausanne team should be thanked for the preshower detector. André Rubbia has been very helpful with his calorimeter package which has been used for this analysis as well as occasional discussions on various issues.

I would like to thank all those who worked on the data-acquisition with me, both from inside NOMAD and from the ECP/DS division at CERN. I would also like to thank Nancy Anderson and Janet Krupsaw from the physics department for trying to keep my paperwork straight. Finally, I would like to thank Nina Madsen for her numerous readings, suggestions and for all the support she has showed for me during the whole process.

Contents

List of Figures

Chapter 1

Introduction

Neutrino physics continues to generate a high level of interest, not only among high-energy physicists, but among cosmologists and astronomers as well. One may certainly attribute part of this to the fact that neutrinos are less understood than their charged lepton counterparts; for those in the astrophysics sector the possibility that neutrinos may have a non-zero mass is intriguing since this could provide a possible solution to the problem of the "missing mass" of the universe. It is with that spirit in mind, that I have pursued this analysis.

1.1 Motivation

The *standard model*, via the group $\mathrm{SU(3)} \times \mathrm{SU(2)_L} \times \mathrm{U(1)_Y}$, attempts to describe, in a single theory, the strong and electroweak interactions of elementary particles. This model, which has withstood many experimental challenges over the years, remains the most predictive tool we have in particle physics. The theory groups quarks and leptons into scalar fields represented by SU(2) doublets, i.e. the

$$\begin{pmatrix} u \\ d \end{pmatrix}, \begin{pmatrix} c \\ s \end{pmatrix}, \begin{pmatrix} t \\ b \end{pmatrix}$$

quark doublets and the

$$\begin{pmatrix} \nu_e \\ e \end{pmatrix}, \begin{pmatrix} \nu_\mu \\ \mu \end{pmatrix}, \begin{pmatrix} \nu_\tau \\ \tau \end{pmatrix}$$

lepton doublets. The theory assumes, implicitly, that neutrinos have no mass, that they are "left-handed," and that neutrino flavor is conserved. An experimental discovery which violates any of these assumptions would be "beyond" the standard model.

In 1991, the NOMAD experiment was proposed [2] at CERN to search for $\nu_\mu \rightarrow \nu_\tau$ oscillations in a wide-band ν_μ beam using kinematic criteria to "observe" the decay of the τ^-. Physics data-taking began in May 1995. While the oscillation analysis is the primary goal of the NOMAD experiment, that does not exclude research into other physical phenomena. In 1995, the KARMEN Collaboration published a report,[1] where they attempt to explain

an observed anomaly in their time spectrum for π^+ decays. In this report, they hypothesize the existence of a rare decay,

$$\pi^+ \to \mu^+ + \mathcal{X}^0$$

where $\mathcal{X}^0$ is some unknown, massive, neutral particle. One possible interpretation of the $\mathcal{X}^0$ is a neutrino excited state (ν^*). Such a discovery, if confirmed, would indicate that neutrinos have mass. Even if the unknown particle were to turn out not to be a neutrino, it would nevertheless have a profound impact on our understanding of elementary particles. The purpose of this analysis is to set limits on this phenomenon using the NOMAD neutrino detector at the CERN SPS accelerator.

1.2 Experimental Method

In order to search for the rare decay mentioned above, one needs a copious source of pions. The CERN wide-band neutrino beam line provides this; approximately eight times per minute, $\sim 10^{13}$ protons hit a beryllium target producing ten to twenty times this number of secondary particles — mostly π^+ and K^+. The particles are focused magnetically and then pass through a long tunnel in vacuum. There is some probability that the π^+ will decay in this tunnel. If a rare π^+ decay mode, as proposed above, exists; then some

small fraction of them will decay to $\mathcal{X}^0$. Assuming that the $\mathcal{X}^0$ has a very low interaction cross-section, it is quite likely to pass unperturbed through the material after the decay tunnel. Since the $\mathcal{X}^0$ is massive, it will decay exponentially with some characteristic lifetime, τ. Thus, some fraction of the $\mathcal{X}^0$ should survive up until the NOMAD detector. Of those, some will decay inside the detector itself. By examining the number of single photons observed in the detector at very low angle with respect to the beam and scaling it for efficiencies and the flux of neutrinos, one can obtain a limit on the branching ratio for the decay $\pi^+ \to \mu^+ + \mathcal{X}^0$ (assuming exclusive decay via the channel $\mathcal{X}^0 \to \nu + \gamma$) as a function of the $\mathcal{X}^0$ lifetime. In scenarios where other decay modes of the $\mathcal{X}^0$ are significant, the limit would have to be scaled.

Chapter 2

Models for the $\mathcal{X}^0$

In some subfields of particle physics, certain paradigms result in a single theory against which experimental observations are compared and contrasted. With the report of any new, unexpected observation comes a flurry of theoretical explanations. Some will fit into the established paradigm; others will require entirely new models. Since a number of models attempt to explain the KARMEN anomaly, a small compendium of current explanations is presented.

The KARMEN collaboration reported[1] an anomaly in the time distribution of neutrinos from a pulsed beam-stop source. They hypothesized this to be due to to the presence of an unknown, weakly-interacting neutral particle emitted in π^+ decay — i.e.

$$\pi^+ \to \mu^+ + \mathcal{X}^0$$

with a mass

$$M_{\mathcal{X}^0} \quad = \quad 33.9 \quad \mathrm{MeV/c^2}.$$

At the "Neutrino 96" conference, KARMEN reported that they see:

$$112 \quad \pm \quad 32 \quad \text{events}$$

in the anomaly, corresponding to an almost 4σ deviation from expectation [3]. Several possible models for the $\mathcal{X}^0$ have been proposed. They include:

1. an isodoublet characterization with the dominant component being the ν_τ (as discussed by various authors), [4, 5, 6]
2. a mainly-isosinglet (sterile) neutrino, [4, 5, 7, 8] and
3. a light photino ($\tilde{\gamma}$) which decays radiatively due to R-parity violation. [9]

The choice of model for the $\mathcal{X}^0$ has some consequences since it will determine the branching ratio for the decay channel $\mathcal{X}^0 \to \nu + \gamma$ for which this analysis searches.

2.1 The Isodoublet Interpretation

The most obvious interpretation of the $\mathcal{X}^0$ is as a heavy sequential neutrino — i.e. ν_3 with dominant contribution from the ν_τ. This scenario is disfavored by some theorists [4], since recent measurements by ALEPH [10] using the decay

$\tau^- \to 5\pi(\pi^0) + \nu_\tau$ give

$$M_{\nu_\tau} < 24 \text{ MeV} \quad \text{(ALEPH)}$$

to conclude that the ν_τ cannot be the main component of the $\mathcal{X}^0$. Additionally, they argue that if the $\mathcal{X}^0$ has "standard" weak interactions and has a lifetime of less than $\sim 10^8$ seconds, the resulting cosmological relic abundance would be significant enough that its decay products would distort the 2.73 K blackbody radiation background. With a lifetime of more than 10^8 seconds, the $\mathcal{X}^0$ does not fall into the sensitive range of the KARMEN experiment, and thus cannot explain the anomaly. Proponents of this solution point out that the rejection of this solution on the grounds of the ν_τ mass limits is flawed since the possibility of neutrino mass mixing is not properly taken into account, particularly for three-flavor mixing scenarios. [6]

2.2 The Mainly-isosinglet (Sterile) Neutrino Interpretation

A much preferred solution is the mainly-sterile neutrino scenario. The "sales pitch" for this model includes that it:

- accepts Dirac or Majorana options,

- works within narrow bounds on mixing parameters,
- has fewer cosmological and astrophysical problems,
- should be seen at the LSND experiment at LAMPF, and
- has two "visible" channels, $\mathcal{X}^0 \to e^+ + e^- + \nu$ and $\mathcal{X}^0 \to \nu + \gamma$.

Letting $U_{\alpha i}$ represent the usual mixing matrix with ν_{iL} representing the mass eigenstates where $\alpha \in [e, \mu, \tau]$ and $i \in [1, 2, ..., N_{mass\ eigenstates}]$:

$$\nu_{\alpha L} = \sum_i U_{\alpha i} \nu_{iL}$$

one can write the branching ratio in terms of $|U_{\mu \mathcal{X}^0}|^2$:

$$\frac{\Gamma(\pi \to \mu \mathcal{X}^0)}{\Gamma(\pi \to \mu \nu)} = \frac{|U_{\mu \mathcal{X}^0}|^2 \left[m_\pi^2 (m_\mu^2 + m_{\mathcal{X}^0}^2) - (m_\mu^2 - m_{\mathcal{X}^0}^2)^2 \right] \lambda^{\frac{1}{2}}(m_\pi^2, m_\mu^2, m_{\mathcal{X}^0}^2)}{m_\mu^2 (m_\pi^2 - m_\mu^2)^2}$$

where $\lambda(a, b, c) = a^2 + b^2 + c^2 - 2ab - 2bc - 2ca$. Then, the width of the two "detectable" decay modes of the $\mathcal{X}^0$ are [4, 5]:

$$\begin{aligned} \Gamma(\mathcal{X}^0 \to e^+ e^- \nu) &= 390K[(1 + 4\sin^2\theta_W + 8\sin^4\theta_W)|U_{e\mathcal{X}^0}|^2 \\ &\quad + (1 - 4\sin^2\theta_W + 8\sin^4\theta_W)(|U_{\mu\mathcal{X}^0}|^2 + |U_{\tau\mathcal{X}^0}|^2)] \ \mathrm{s}^{-1} \\ \Gamma(\mathcal{X}^0 \to \nu\gamma) &= 390K \left[\tfrac{27\alpha}{8\pi} (|U_{e\mathcal{X}^0}|^2 + |U_{\mu\mathcal{X}^0}|^2 + |U_{\tau\mathcal{X}^0}|^2) \right] \mathrm{s}^{-1} \end{aligned}$$

so that the "visible" width is obtained by summing the two and the total width is obtained from another paper [7]:

$$\begin{aligned} \Gamma_{\text{visible}} &= K[920|U_{e\mathcal{X}^0}|^2 + 210|U_{\mu\mathcal{X}^0}|^2 + 210|U_{\tau\mathcal{X}^0}|^2] \quad \mathrm{s}^{-1} \\ \Gamma_{\text{total}} &= K[2470|U_{e\mathcal{X}^0}|^2 + 1760|U_{\mu\mathcal{X}^0}|^2 + 1760|U_{\tau\mathcal{X}^0}|^2] \quad \mathrm{s}^{-1} \end{aligned}$$

where $K = 1(2)$ for Dirac (Majorana) neutrinos, respectively. The non-visible modes are principally decays like $\mathcal{X}^0 \to \nu\nu\nu$. One can see that for visible decays in the mainly-sterile neutrino scenario, $\mathcal{X}^0 \to e^+ + e^- + \nu$ will always dominate over $\mathcal{X}^0 \to \nu + \gamma$. How much it dominates, however, will depend on whether $|U_{\mu\mathcal{X}^0}|^2 + |U_{\tau\mathcal{X}^0}|^2$ dominates Γ_{visible} or if it is instead $|U_{e\mathcal{X}^0}|^2$. i.e. as one increases $|U_{\mu\mathcal{X}^0}|^2 + |U_{\tau\mathcal{X}^0}|^2$, the fraction of $\mathcal{X}^0 \to \nu + \gamma$ will increase.

2.3 The Radiatively-decaying, R-Parity Violating, Light Photino Interpretation

A recent paper [9] proposes a supersymmetric solution, where the $\mathcal{X}^0$ is a light photino ($\tilde{\gamma}$). This scenario assumes the minimal supersymmetric standard model (MSSM) with the $\tilde{\gamma}$ as the lightest supersymmetric particle. This hypothesis has the advantages that it:

- is consistent with all experimental data,
- generates no problems with cosmological nucleosynthesis, and
- can be constrained to accommodate SN 1987A neutrinos.

Let's consider the MSSM model. The decay

$$\pi^+ \to \mu^+ + \tilde{\gamma}$$

clearly does lend itself to a simple supersymmetrization of the standard model Lagrangian, but rather requires something more complex. In order to avoid terms (couplings) which violate symmetries like Baryon or lepton number, a discrete symmetry called *R-parity* in introduced. It is given by:

$$R = (-1)^{3B+L+2S}$$

where B, L, and S represent the baryon number, lepton number, and intrinsic spins of the field, respectively. However, having **exact** R-parity, albeit aesthetically pleasing, is not strictly necessary; as long as such couplings do not violate experimental results, they should be allowed.

Violation of R-parity is necessary in this scenario in order for the lightest supersymmetric particle, the $\tilde{\gamma}$, to decay as well as for it to be produced via $\pi^+ \to \mu^- + \tilde{\gamma}$. In the simplest version of this interpretation, only one coupling is R-parity violating; its strength being given by λ'_{211}. (This coupling violates lepton number as well.) In this case, the radiative decay mode will dominate: $\tilde{\gamma} \to \nu_\mu + \gamma$ with a branching ratio given by:

$$\frac{\Gamma(\pi^+ \to \mu^+ \tilde{\gamma})}{\Gamma(\pi^+ \to \mu^+ \nu_\mu)} = \frac{8\pi}{\alpha} \left(\frac{\lambda'_{211} \sin^2 \theta_W m_\pi^3}{m_u + m_d} \right)^2 \frac{m_W^4}{m_{sq}^4} \frac{m_\pi^2 - m_\mu^2 - m_{\tilde{\gamma}}^2}{m_\mu^2 (m_\pi^2 - m_\mu^2)^2} \mathcal{C} \left(1, \frac{m_{\tilde{\gamma}}^2}{m_\pi^2}, \frac{m_\mu^2}{m_\pi^2} \right)$$

where $\mathcal{C}(a,b,c) \equiv [(a-b-c)^2 - 4bc]^{\frac{1}{2}}$ and where the squark masses are degenerate, i.e. $m_{sq} = m_{\tilde{u_L}} = m_{\tilde{d_L}} = m_{\tilde{d_R}}$. The photino decay width is then:

$$\Gamma \equiv \Gamma(\tilde{\gamma} \to \nu_\mu \gamma) = \frac{\alpha^2 \lambda'^2_{211}}{2592\pi^3} \frac{m_{\tilde{\gamma}}^3}{m_{sq}^2} f\left(\frac{m_d^2}{m_{sq}^2} \right)$$

where

$$f(x) = x\left[1 + \frac{3 - 4x + x^2 + 2\ln x}{(1-x)^3}\right]^2$$

This solution allows agreement with KARMEN for a large range of R-parity violating couplings and squark masses. Forcing the squark masses to be degenerate resolves conflicts with SN 1987A data. With this scenario, the limit curves in chapter 8 need not be adjusted since, there, it is assumed that $\Gamma \equiv \Gamma(\tilde{\gamma} \to \nu_\mu \gamma)$.

There are, no doubt, other models which could explain this phenomena. However, these are the ones which are being widely considered in theoretical circles at the time of this publication.

Chapter 3

The Neutrino Beam

Neutrino physics experiments may be divided into a variety of categories: accelerator, reactor, solar, atmospheric, etc.... Some, like solar and atmospheric neutrino experiments depend on neutrinos produced outside the realm of the experiment; others, like accelerator and reactor experiments, use some apparatus to generate a large flux of neutrinos within certain energy ranges. Accelerator-based experiments generate neutrinos as the decay products of secondary particles which result from a proton beam incident on some target. Other particles which result from these decays are eliminated downstream either by forcing them to "range out" by passing through some large quantity of dense material like iron or earth, or by being deflected in some magnetic field so that they miss the experimental setups.

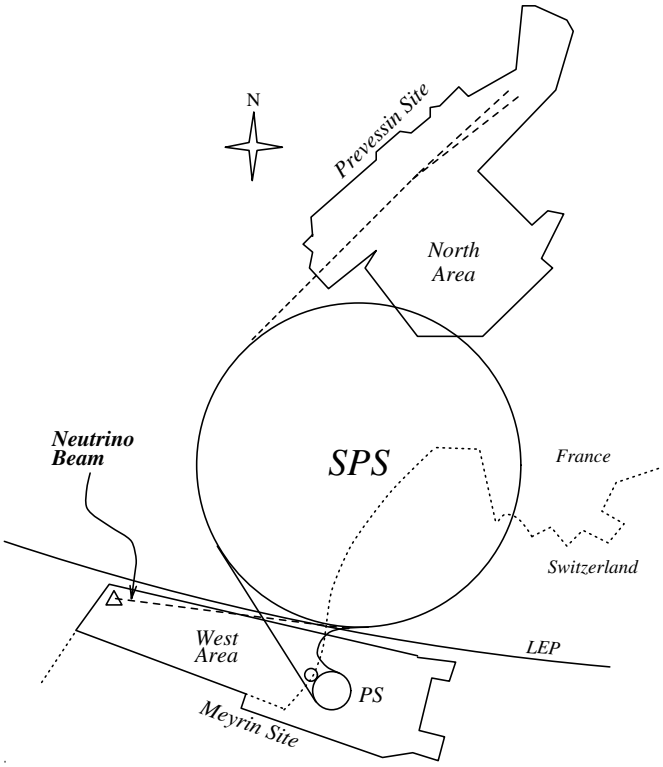

Figure 3.1: The CERN Accelerator Complex - NOMAD is at the triangle

The SPS accelerator at CERN generates a 450 GeV proton beam used in generating a neutrino beam as well as for a variety of other experiments[11]. The configuration[12] of the accelerators is shown in figure 3.1.

The SPS accelerates protons and extracts the resulting beams for experiments once every 14.4 seconds. Two bursts of 2.5×10^{13} protons arrive at the SPS from the smaller CERN accelerator, the PS. They are accelerated from a few tens of GeV to 450 GeV at which point they are extracted and steered onto various targets. Typically, $\sim 3.2 \times 10^{13}$ protons remain after acceleration

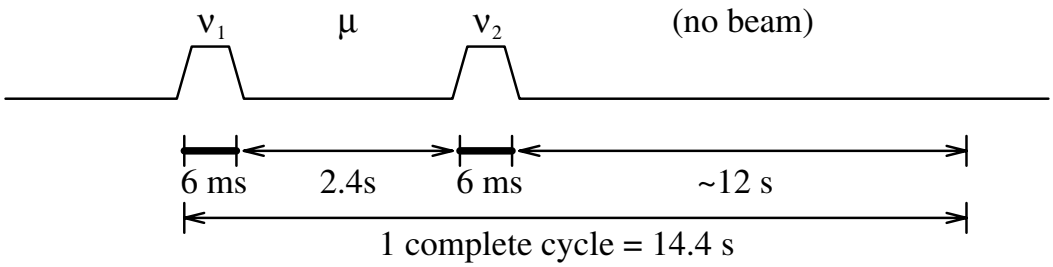

Figure 3.2: The Structure of the SPS Cycle

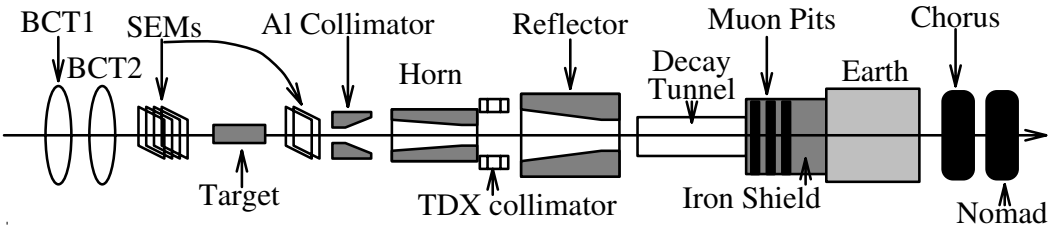

Figure 3.3: A Schematic Layout of the CERN Neutrino Beam Line. (Not drawn to scale)

and extraction. As shown in figure 3.2, the first neutrino extraction (ν_1) of $\sim 1.2 \times 10^{13}$ protons occurs within a six millisecond period followed by an extraction of 0.8×10^{13} protons for other fixed-target experiments during the 2.4 second "flat-top." The remaining $\sim 1.2 \times 10^{13}$ protons form the second neutrino extraction (ν_2). The neutrino extraction is split into two pieces to allow the production target to cool down. Due to the very low interaction cross-section of neutrinos, only a few neutrino events are induced at the experiments during each extraction. As a result, the neutrino extractions have

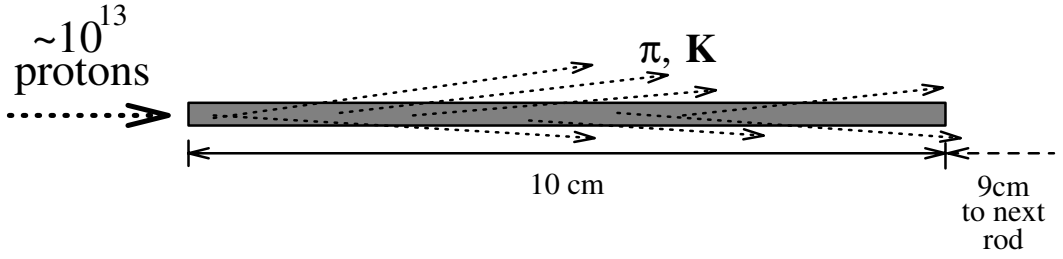

Figure 3.4: One of the Eleven Beryllium Rods that Make Up the Target

been deliberately kept as short as possible to minimize the effect of cosmic rays.

Protons from the neutrino extractions pass into the neutrino "cave" where they collide with a production target. Figure 3.3 shows a simple diagram of the cave and the areas downstream.[13] The target consists of a series of eleven collinear rods, each of which is ten cm in length and three mm in diameter. Each rod is separated from the next by a nine cm gap. Protons pass through the rods generating secondary particles (π and K). Immediately after the target, they pass through a large-angle aluminum collimator which absorbs most of the secondary particles which are outside of the acceptance of the decay tunnel; this prevents unnecessary irradiation of the later areas of the beamline. Eight meters downstream, two magnetic devices, the "horn" and the "reflector" pulse at over 100 kiloamps in-time with the beam in order to focus charged secondaries before they pass into the decay tunnel. Between

the horn and the reflector lies the iron (TDX) collimator which helps absorb particles which would generate more $\overline{\nu}$ contamination in the beam.[1] This 290 meter long tunnel, which is kept under vacuum, allows decays like[14]

$$\pi^+ \rightarrow \mu^+ + \nu_\mu,$$

$$K^+ \rightarrow \mu^+ + \nu_\mu, \quad and$$

$$K_L \rightarrow \pi^- + \mu^+ + \nu_\mu.$$

Afterward, all particles except neutrinos and some muons quickly range-out in a series of iron walls and earth. Silicon detectors placed in special pits amidst the iron and earth shielding provide some measure of the muon flux and hence the neutrino beam profile. Additional earth and a final series of magnetic toroids eliminate most of the remaining muons resulting in a neutrino beam. Here are a few additional numbers describing the beam line:[15]

Beam Layout Numbers	
distance from target to start of decay tunnel	124 m
distance from target to horn	18.9 m
distance from target to reflector	90.4 m
length of decay tunnel	290 m
length of iron shield	324.5 m
length of earth "shield"	144 m
distance from target to NOMAD	838.5 m
interaction lengths for target	2.7 λ

[1]The fact that protons are positively charged results in a higher probability that positive fragments are "leading", i.e. that they carry most of the p_L. Consequently, π^+ and other positive particles which decay into ν rather than $\overline{\nu}$ will have angular spectra which are peaked toward much smaller angles, thus missing the TDX collimator.

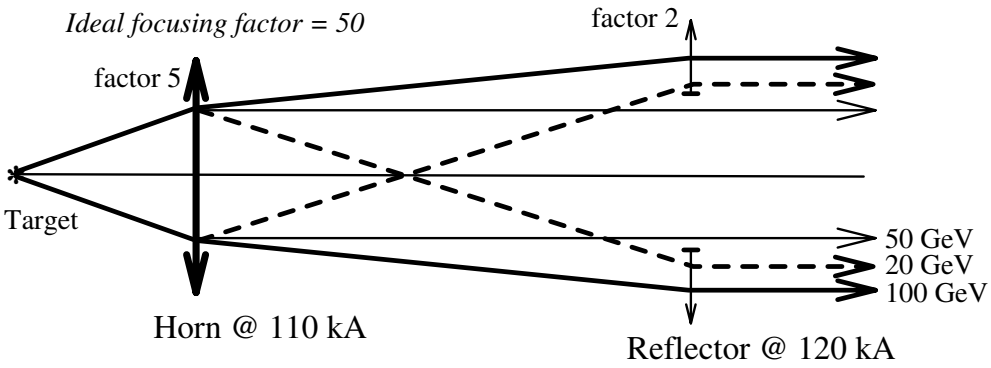

Figure 3.5: A Schematic Showing the Principle of the Horn and Reflector

One can consider the horn and reflector as an analog of a two-lens optics experiment where one tries to focus the light from a pinpoint source at infinity. In such an ideal case, the neutrino intensity would be a factor fifty more intense than without the horn and reflector. However the analogy is not perfect, since the target in not a point but two meters in length, the apparati are not completely transparent to the passing particles and the horn and reflector should be treated as thick, rather than thin, lenses; in practice, an intensity amplification of about ten is observed. A simple schematic is shown in figure 3.5.

The above reactions are obviously not the only ones which occur in the decay tunnel and in addition to some muon contamination, there is some contribution to the beam from various other types of neutrinos, notably $\overline{\nu_\mu}$ and ν_e whose presence must be properly simulated for most physics analyses

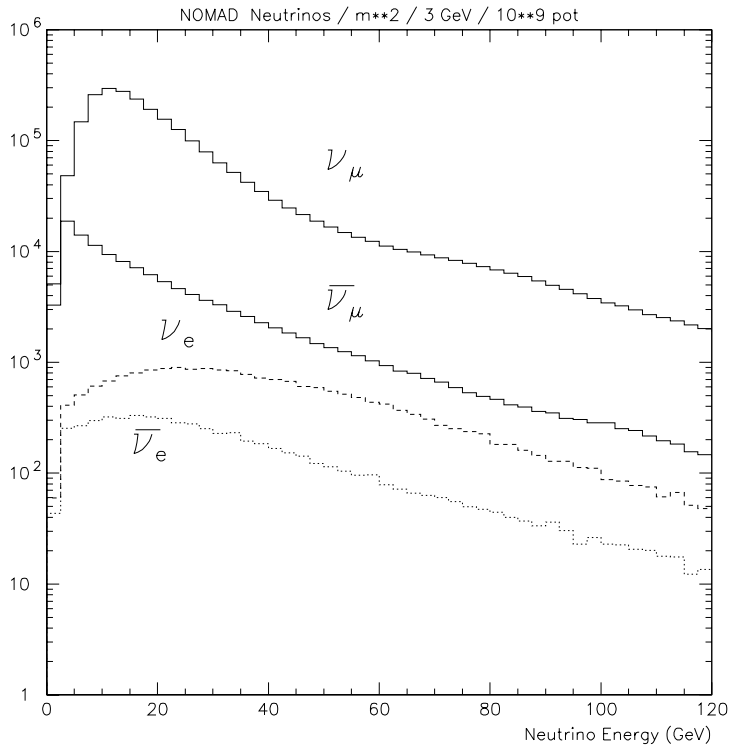

Figure 3.6: Neutrino Flux at NOMAD from Monte Carlo Normalized to Protons Incident on the Target (POT) (Note log scale)

on NOMAD. The absolute flux versus energy for neutrinos which pass through NOMAD is shown in figure 3.6.

Information regarding physics processes and the simulation of the beam may be found in the Monte Carlo chapter.

Chapter 4

The Neutrino Detector

The design of the NOMAD neutrino detector includes the elements required for the primary task of searching for $\nu_\mu \to \nu_\tau$ oscillations using kinematic criteria while maintaining adequate flexibility to allow the pursuit of other physics analyses as well as future upgrades of the detector. The detector contains the following parts or *sub-detectors:*

- the magnet,
- the veto scintillators,
- the forward calorimeter,
- the drift chambers,
- the transition radiation detector or *TRD*,
- the trigger scintillators,
- the preshower,
- the electromagnetic calorimeter,

- the hadron calorimeter,
- and the muon chambers.

Some of these detectors are, themselves, upgrades of the original proposal[2]. These include the forward calorimeter and the hadron calorimeter. Data and tables describing the sub-detectors are taken from a NOMAD collaboration internal note[16] unless otherwise noted.

4.1 The Magnet

Measurement of charged particle momenta, particularly near the primary interaction vertex, is essential to most NOMAD analyses. This is achieved by tracking the particles through a magnetic field. For this purpose, we have recuperated the magnet from the UA-1 experiment at CERN. I have summarized its properties in the following table:

Salient Features of the NOMAD Magnet	
magnet material	aluminum
return-yolk material	iron
average field	0.4 tesla
field homogeneity (center)	$\sim 2\%$
field homogeneity (near edge)	$\sim 10\%$

The drift chambers, transition radiation detector, trigger, preshower, and electromagnetic calorimeter lie inside the magnet; the veto and the muon

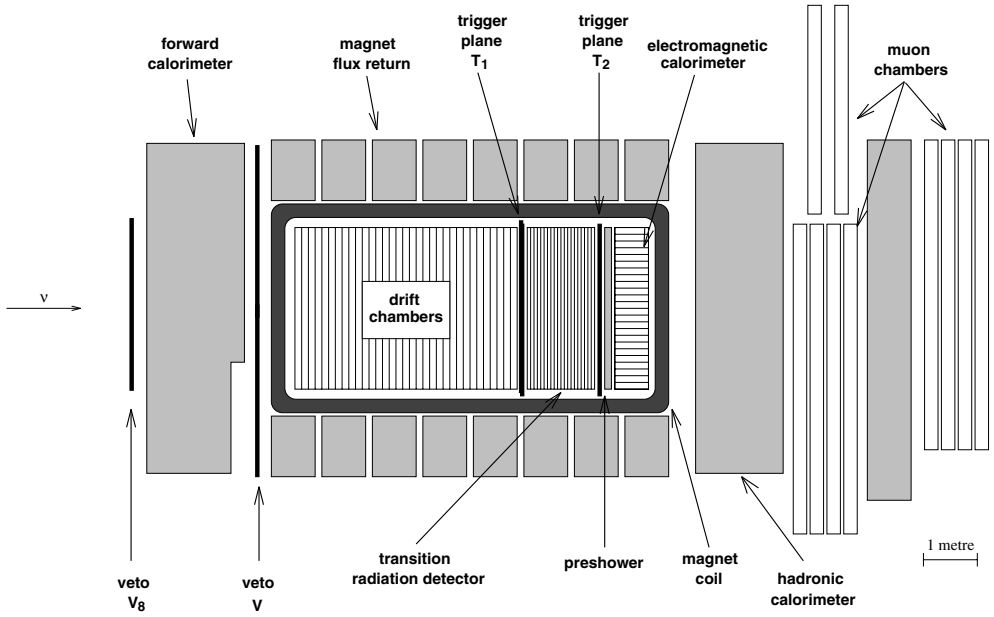

Figure 4.1: The NOMAD Detector

chambers lie outside this volume, while the forward and hadronic calorimeters are embedded in the iron flux-return as shown in figure 4.1.

4.2 The Veto Counters

In order to help eliminate events which result from interactions outside the fiducial volume of the detector as well as background from cosmic rays, veto counters have been mounted on the outside of the "upstream"-end of the iron return yoke of the magnet. The veto consists of a series of horizontal and vertical scintillators read-out by photo-multiplier tubes on both ends. Some characteristics of the veto counters are summarized below:

"What nots" of the Veto Counters	
active veto area	23.642 m^2
number of scintillators (long)	38
number of scintillators (short)	15
typical efficiency	96.5-97.5 %
time resolution	0.3 ns
dead-time due to veto	$\sim$3%

The signals from the fifty-three counters are properly discriminated and then OR-ed to form the veto. The absence of any signal from these counters is required in coincidence with the trigger scintillators for the standard neutrino trigger.

4.3 The Forward Calorimeter

After passing the veto counters but before reaching the first part of the active target volume, neutrinos pass through a series of slotted-iron slabs which form the upstream part of the flux return for the magnet. In the UA-1 experiment, these slots were instrumented with scintillation counters in order to make a simple hadronic calorimeter. A similar sub-detector called the forward calorimeter or *FCal* was added for the 1995 run with the motivations of looking for $\nu_\mu - CC$ interactions generating multiple muons in the final state and of searching for neutral, heavy particles produced in neutrino interactions. Included below are interesting FCal numbers; additional details are available

from other notes. [17]

FCal Numbers	
FCal target mass	17.7 tons
iron plates	23
depth of iron plate	49 mm
slots	22
depth of slots	18 mm
instrumented slots	20
scintillator rows	10
photo-multiplier channels	20
scintillator length	185 cm
scintillator height	18.5 cm
depth of coverage	134 cm
interaction lengths	5.5λ

4.4 The Drift Chambers

The "traditional" method for the construction of drift chambers requires some large, usually aluminum, support structure. In a neutrino experiment, where a large amount of target material is required and the interaction location is not well-defined, proper determination of the vertex location requires many repeated layers of target material and drift chambers. The disadvantage of this is that the tracking and vertex algorithms must then deal with the multiple scattering which occurs before the charged tracks coming from the primary vertex reach active tracking volume.

In NOMAD, the drift chambers are made of a "self-supporting" material, so that the support structures can be removed; the target mass becomes the walls of the drift chambers themselves.

The structure is, to a fair approximation, carbon. By choosing a material which has a low atomic number or Z, the radiation length of the drift-chamber region can be minimized increasing the probability that electrons (and photons) reach the TRD and ECal regions where one can identify them.

The planes of wires are arranged at $-5°$, $0°$, and $+5°$ with respect to the magnetic field, referred to as u, y, and v wires respectively. Four aramid-fiber planes "sandwich" one complete set of three planes to form a *chamber*. For mechanical and installation reasons, the vast majority of the chambers are packaged together into groups of four to form a *module*. A few pertinent quantities are summarized below:

The Finer Points of the Drift Chamber	
width covered	300 cm
height covered	300 cm
depth covered	400 cm
fiducial mass	2.57 tons
number of y wires	44
number of u and v wires	41
wire spacing	6.4 cm
wall thickness	1.6 cm
drift gap	0.8 cm
drift gas mixture	60% ethane, 40% argon
radiation length	0.02 X_0 per chamber
y resolution	$\sim$250 μm per plane
x resolution	$\sim$1500 μm per chamber

The design of the drift chambers, while one of the most important differences of NOMAD and other neutrino experiments, have also proven to be its most problematic detector component. In 1992, construction difficulties delayed their scheduled completion date by one year, so that the chambers would not be completely installed by the beginning of running in 1994. When the chambers were eventually installed and put into operation, they slowly began to develop structural problems inside due to an unfortunate choice of adhesive during construction. This caused most of the chambers to become unusable by the latter part of the year so that the data taken in 1994 became essentially unusable for physics purposes. After extensive repair and modification operations starting in late 1994 and finishing by the middle of 1995, the chambers finally performed as originally designed. One should note that

for 1995, chambers were re-installed in NOMAD only after they were repaired — i.e. the problems discovered during the 1994 run do not affect any part of the 1995 run. Since my analysis only uses the data taken during 1995, the adhesive problem does not result in any reduction in the quality of the drift chamber information used in my analysis.

4.5 The Transition Radiation Detector

In order to be able to perform the search $\nu_\mu \to \nu_\tau$ oscillations using the decay process $\tau^- \to e^- \bar{\nu}_e \bar{\nu}_\tau$, one needs to distinguish π^- from e^- with relatively high efficiency. NOMAD accomplishes this with the transition radiation detector or *TRD*. TRDs use the fact that charged particles emit radiation when passing from one medium to another with different electromagnetic properties. The choice of material or *radiator* as well as its geometry are designed to maximize the intensity of this radiation as illustrated in figure 4.2. One places "straw" tubes or similar simple detectors just after the radiators to detect these photons. Detailed explanations of the physics involved may be found elsewhere.[18]

The TRD as used in NOMAD consists of nine planes of "foil" radiators each of which is followed by a series of vertical straw tubes. Here are some important TRD numbers:

Figure 4.2: TRD Signal for e^-

Important TRD Numbers	
radiators	9
foils per radiator	315
foil material	polypropylene
foil thickness	15μm
gap between foils	250 μm
total radiation length radiators	.1 X_0
straw tube planes	9
straw tubes per plane	176
inside diameter of a tube	1.6 cm
wire material	tungsten
gas in tubes	75% xenon, 25% methane
tube material	aluminized mylar

Altogether, the e/π rejection factor given by the TRD is $\sim 10^3$.

4.6 The Trigger Scintillators

The normal NOMAD neutrino oscillation trigger consists of two planes of scintillation counters placed at the beginning and end of the TRD region. Each plane is divided into left and right half-planes, each of which consists of fourteen horizontal counters. Each counter is read-out on one side only. Two additional counters have been placed vertically along the light-guides of the horizontal counters in order to increase the fiducial area.

The Trigger in Essence	
total area covered	286.0 cm × 286.0 cm
size of horizontal counters	124.0 cm × 19.9 cm × 0.5 cm
size of vertical counters	130.0 cm × 19.9 cm × 0.5 cm
position of first plane	z = 408.3 cm
position of second plane	z = 569.3 cm
efficiency per counter	∼98%

Note that the plane positions refer to the start of the fiducial region, i.e. the front face of the first drift chamber.

4.7 The Preshower

In order to help pinpoint the development of electromagnetic showers in the detector, a "preshower" detector has been installed in the region just upstream of the electromagnetic calorimeter. The preshower consists of two Pb-Sb sheets

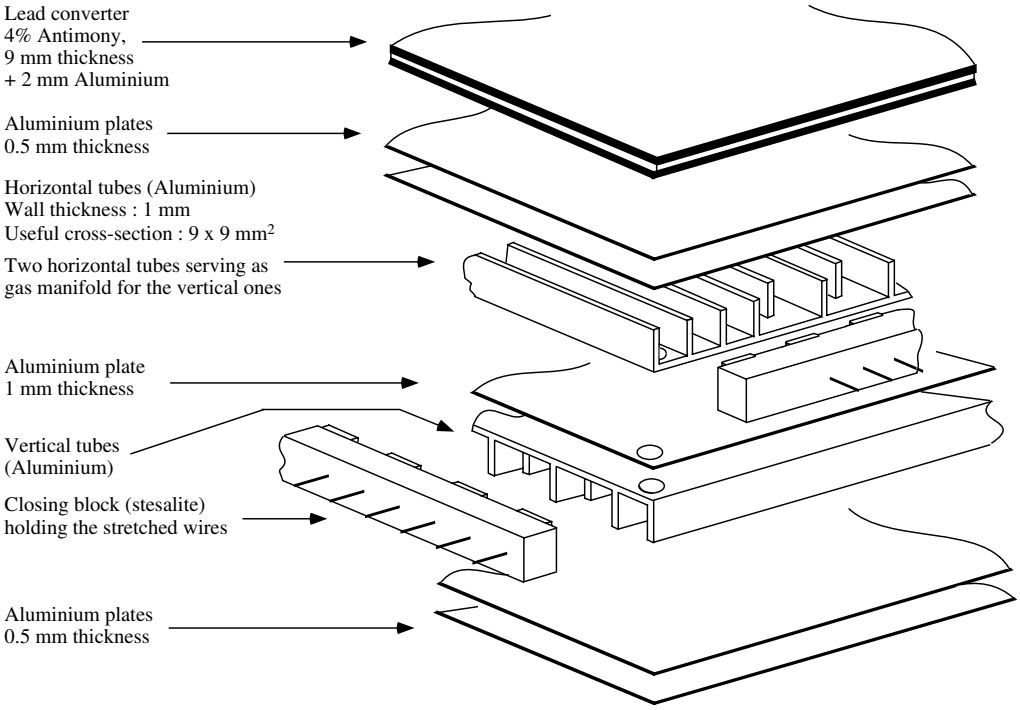

Figure 4.3: Cut-away View of the Preshower

(96% lead, 4% antimony by weight) supported by a 2.0 mm thick Al sheet; this is followed by two planes of proportional streamer tubes — one horizontal and one vertical. In addition to the normal charged particles, one should also be able to identify photons since they have a high probability to pair-produce in the lead sheet. A cut-away view is show in figure 4.3. Additional characteristics include:

The Preshower — Up Front	
tubes per plane	290
total area covered	292.1 cm × 290.1 cm
tube cross-section	1.0 cm × 1.0 cm
thickness of tube wall	0.5 mm
thickness of each Pb sheet	0.45 cm
front face of Pb position	z = 575.8 cm
gas mixture	80% Argon, 20% CO_2
radiation length	1.6 X_0
interaction length	0.05 λ

As an artifact of the manufacturing process, four of the horizontal tubes and two of the vertical tubes are not instrumented.

Energy deposition in the preshower for $e^{\pm}$ and $\pi^{\pm}$ are shown in figure 4.4. One can see that the preshower provides an additional means of distinguishing between $e^{\pm}$ and $\pi^{\pm}$; for example, a cut applied at the arrow, rejects all but 8.9% of $\pi^{\pm}$ while continuing to accept 90% of $e^{\pm}$.

4.8 The Electromagnetic Calorimeter

For detecting electromagnetic showers, $PbSiO_2$ (lead-glass) blocks, have proven to be a very good in terms of energy resolution, hermiticity, reliability, and stability.

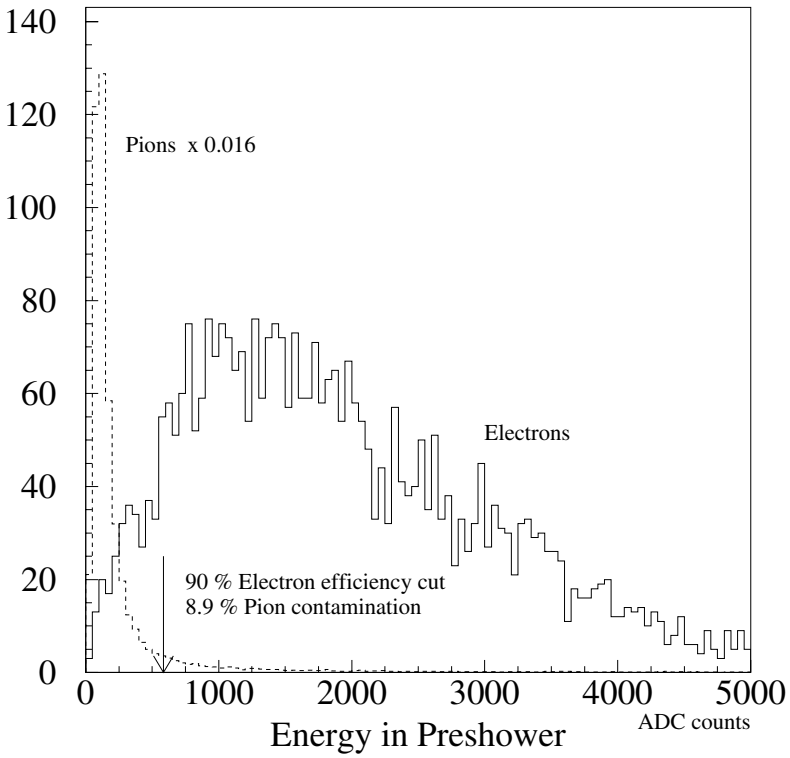

Figure 4.4: Preshower Response in ADC counts (1 count = 0.013 MIPs)

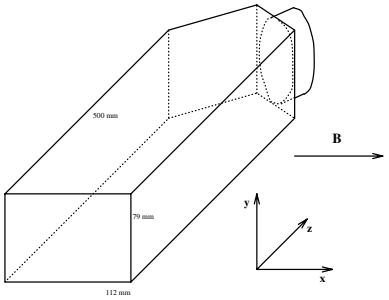

Such a calorimeter, made of lead-glass from Russia, is installed in NOMAD. The ECal, as it is called, consists of a rectangular array of blocks, to each of which is attached a three-inch photomultiplier tube. The photomultipliers are coupled at a 45° angle to the blocks.

The ECal Made Clear	
number of blocks	875
rows × columns	35 × 25
total area covered	280.0 cm × 277.0 cm
block cross section	11.2 cm × 7.9 cm
block length	49.4 cm
front face position	z = 582.3 cm
weight	∼20 metric tons
photoelection/GeV (B off)	∼1200
photoelection/GeV (B on)	∼950
minimum-ionizing signal	0.55 GeV
energy/ADC count	∼25 MeV
radiation length	19.8 X_0
interaction length	1.6 λ

The ECal stability is monitored via two sets of LEDs on opposite corners of the slanted face of each tower. When reading out the signals from the ECal, special electronics have been to designed to select the peak from the signal as opposed to the standard method of charge integration over some time period. The energy resolution thus obtained is

$$\sigma/E = 0.0085 + \frac{0.03}{\sqrt{E(GeV)}}$$

The ECal response to single μ events and to charged-current events is shown in figure 4.5. One can see that muons typically deposit 0.5 GeV with very few events depositing energy in the 1 GeV range. This provides a simple way to identify or reject muons that pass within the ECal's acceptance.

In addition, one type of NOMAD neutrino trigger has been designed to detect neutrino interactions in the ECal which generate energy deposition of

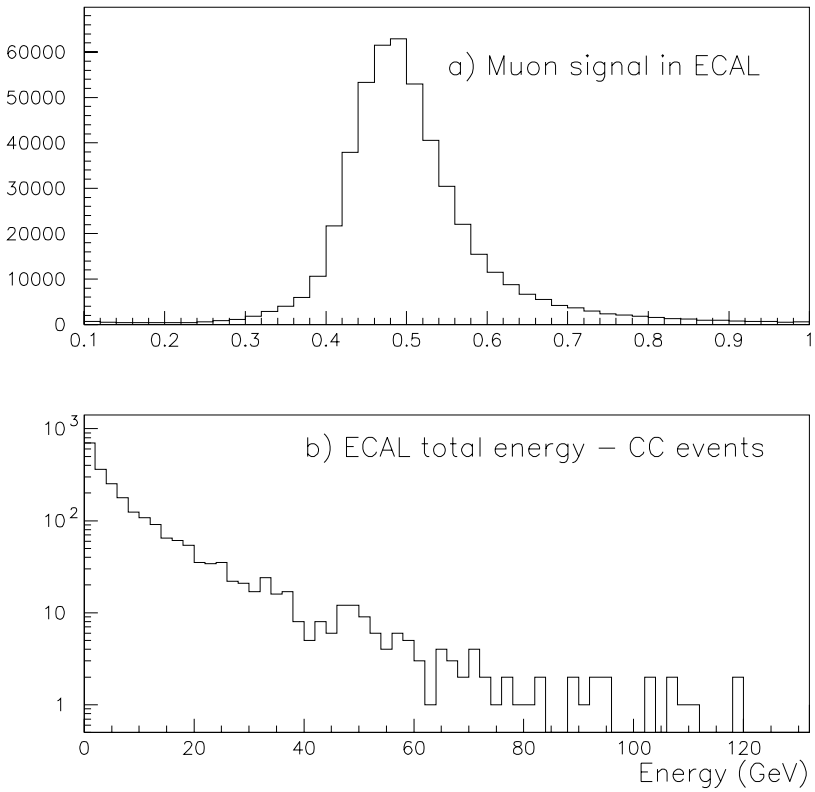

Figure 4.5: ECal Energy Deposition for μ and CC Events

more than 0.60 GeV. The x-y distribution of these events is shown in figure 4.6, giving one a some measure of the shape of the beam inside the detector. Also, using the ECal, NOMAD can reconstruct π^0 by observing two seperated clusters in the ECal, each of which is identified as a photon, thus allowing one to reconstruct the invariant mass as shown in figure 4.7.

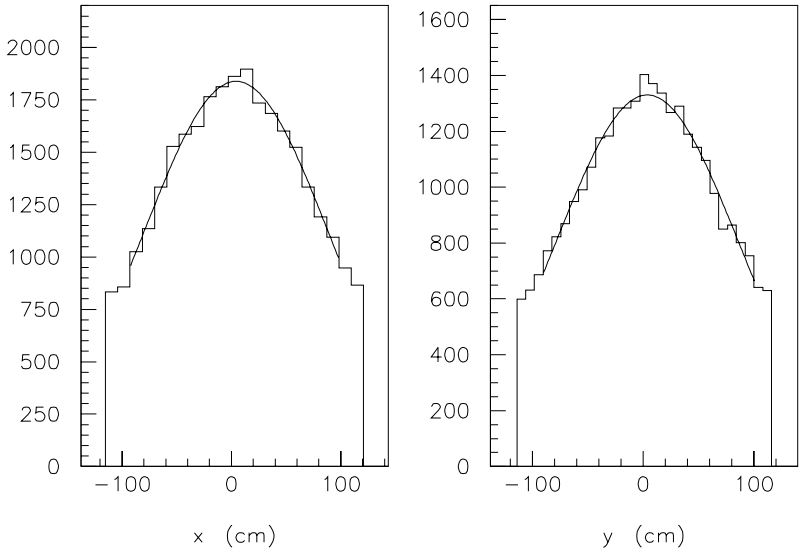

Figure 4.6: X-Y Profile for ν Interactions in the ECal

4.9 The Hadronic Calorimeter

For purposes of hadron detection and as an additional veto against muons, a hadronic calorimeter was installed for the 1995 run. As with the FCal, it consists of eighteen sets of eleven scintillation counters inserted horizontally into successive slots of the rear vertical return yoke of the magnet. A few things of interest:

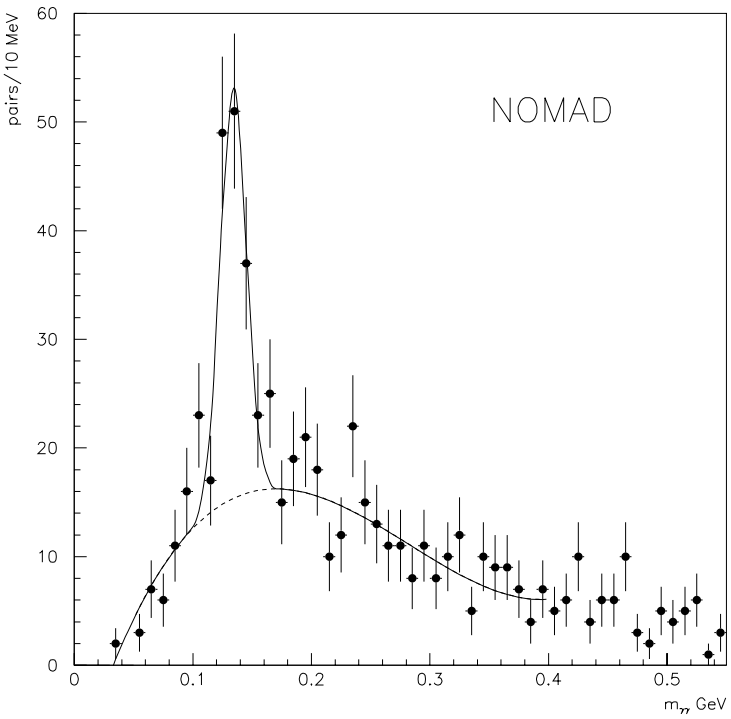

Figure 4.7: The π^0 Mass Peak as Reconstructed in NOMAD

The HCal — All Told	
total area covered	360.0 cm × 350.0 cm
thickness of each plane of iron	4.9 cm
counter length	360.0 cm
counter thickness	1.0 cm
height of normal counters	18.3 cm
height of counters 7 & 8	21.9 cm
height of counter 9	10.6 cm
height of counter 10	13.6 cm
front-face position	z = 710.6 cm
interaction length	3.2 λ

Due to two structural supports which obstruct certain portions of the slots in the rear return yoke, two of the eighteen modules have counters with notches removed; these are modules eight and eleven. Modules seven through ten also have non-standard heights for this reason.

The counters are read out on both sides. The resulting signal is split and both the pulse height and the signal times are measured in order to obtain a very rough estimate on the X position of a hadronic shower in addition to the energy deposited. This simple detector obtains a resolution of

$$\sigma/E \sim \frac{2.0}{\sqrt{E(GeV)}}$$

4.10 The Muon Chambers

Identification of muons is of very high importance in NOMAD; particularly, since a missed muon in a $\nu_\mu - CC$ interaction can result in an event which

mimics a neutrino oscillation signal for one of the main analysis channels. However, NOMAD's needs in this area are not that unusual; so muon chambers from the UA-1 experiment have been recuperated for this purpose.

The NOMAD muon system is comprised of five modules, each of which consists of two chambers — one oriented horizontally and one vertically. These rectangular modules are located such that three of them are in front of an iron absorber wall. Four of the five modules are mounted so that their long axes are vertical, the fifth one being horizontal slightly above the main detector. Here are a few muon chamber numbers:

A Few μ Numbers	
module cross-section	375.0 cm × 555.0 cm
length of long tubes	555.0 cm
length of short tubes	375.0 cm
tube transverse dimensions	14.9 × 4.4 cm
position of module one (x,y,z)	(-172.5 cm, -135.0 cm, 907.3 cm)
position of module two (x,y,z)	(172.5 cm, -135.0 cm, 945.3 cm)
position of module three (x,y,z)	(-172.5 cm, 0.0 cm, 1144.3 cm)
position of module four (x,y,z)	(172.5 cm, 0.0 cm, 1182.3 cm)
position of module five (x,y,z)	(0.0 cm, 363.0 cm, 926.3 cm)
iron wall transverse dimensions	720.0 cm × 640.0 cm
iron wall depth	80.0 cm
gas mixture	40% argon, 60% ethane

In terms of resolution, one obtains 0.25 mm for straight tracks which deteriorates to around 0.50 mm for tracks incident at 40°.

4.11 Triggering

NOMAD has implemented a variety of triggers to study neutrino interactions. They are summarized in the table below:[19]

NOMAD Neutrino Triggers	
$\overline{V}T_1T_2$ (1994-)	Designed to study neutrino interactions in the drift chamber target region, it requires at least one hit the T_1 and T_2 trigger planes. The absence of any veto V signals is required to eliminate single muons.
$\overline{V_8}FCal$ (1995-)	Neutrino interactions in the front calorimeter with an energy deposition of at least 3 MIP fire this trigger. The central portion of the veto V_8 is used to to reject muons.
$\overline{V_8}T_1T_2FCal_2$ (1995-)	This trigger focuses on events that are quasi-elastic in nature. It requires 1 MIP in the FCal. It uses the trigger scintillators in addition to the central veto to insure passage through the detector.
$\overline{T_1T_2}ECal$ (-7/5/1995,1996-)	By placing a threshold of 1.5 MIP on the ECal energy deposition along with the trigger scintillators in anti-coincidence, the ECal is used as a neutrino target. This allows the study of physics topics like $\nu_\mu \rightarrow \nu_e$ and $\nu_\mu \rightarrow \nu_\tau$ oscillations as well as specialized topics like $\mathcal{X}^0 \rightarrow \nu + \gamma$
$\overline{V_{wide}}ECal$ (7/5/1995-end of 1995)	This trigger used an elongated veto signal instead of the trigger scintillators to attempt to improve acceptance. The additional events turned out to be interactions in the magnet and its return yoke; thus NOMAD reverted to $\overline{T_1T_2}ECal$ after 1995.

For this analysis, both the $\overline{T_1T_2}ECal$ and $\overline{V_{wide}}ECal$ triggers were used. These two triggers reach full efficiency at $\sim$1 GeV. The additional $\overline{V_{wide}}ECal$ events

from interactions in the magnet have been removed in the data filtering stage.

In summary, the NOMAD detector has been fully functional since mid-1995 and has experienced no major problems since that time.

Chapter 5

The Data-Acquisition System

There is often a hard-to-dispel impression among experimental particle physicists that the data-acquisition of an experiment is something that can just be "thrown together" with only a minimum of forethought. In reality however, even accelerator-based neutrino experiments, which one might expect to have relatively modest data-taking requirements, need a considerable amount of planning, money, and human effort. NOMAD illustrates this fact quite well.

5.1 Design

The data-acquisition requirements for hardware and software were detailed in memos dating back as early as 1992, only one year after the experiment's original proposal.[20, 21]. At this time, general choices of hardware and software

were made. As NOMAD was to start in a relatively short period of less than two years, the hardware and software were designed to be very hierarchical in order to try to minimize the amount of money and time spent on development.

5.2 Hardware

As described in chapter 3, NOMAD operates in a "burst" mode where many triggers arriving within a few milliseconds and where there are hundreds of milliseconds or even seconds before the next triggers will arrive. In order to minimize dead time, the digitized information is buffered on electronic modules. These modules are situated in a FASTBUS architecture[22]. Widely used in high-energy physics, FASTBUS provides large power supplies, uses large slots allowing considerable complexity in design, and is relatively cheap.

The signals from the various subdetectors arrive at some combination of the following types of FASTBUS modules:

- twelve-bit, sixty-four channel, charge-integrating ADCs (Q-ADC),
- twelve-bit, sixty-four channel, peak-sensing ADCs, and
- sixteen-bit, ninety-six channel, LeCroy Model 1876 TDCs with a one nanosecond resolution.

Both types of ADCs were designed at CERN for NOMAD. The ADCs include

a 256 event memory. The TDCs use a sixty-four kilobyte circular buffer which stores the channels which have been hit. The following table indicates which types of modules are used by the various subdetectors.

FASTBUS Modules Used by Sub-detector			
Sub-detector	**TDCs**	**Q-ADCs**	**Peak-ADCs**
drift chambers	•		
TRD		•	
preshower		•	
trigger	•		
veto	•		
FCal	•	•	
HCal	•	•	
ECal			•
muon chambers	•		

There are a maximum of 11648 channels to readout per event for all of NOMAD.

The weak-point of FASTBUS, however, has always been the FASTBUS *masters* which control the crates and the inter-crate connectivity. As an alternative to standard FASTBUS, five VME-based 6U boards, built by CES in Geneva, Switzerland, using Motorola 68040 processors control the readout of the front-end electronics through an extended VME Subsystem Bus (VSB) connected to slave controllers in each of the twelve FASTBUS crates used by NOMAD as shown in figure 5.1. Each of the FASTBUS controllers provide four megabytes of additional memory for event buffering. The VME controllers perform block transfers of the available data to local buffers, assemble the data

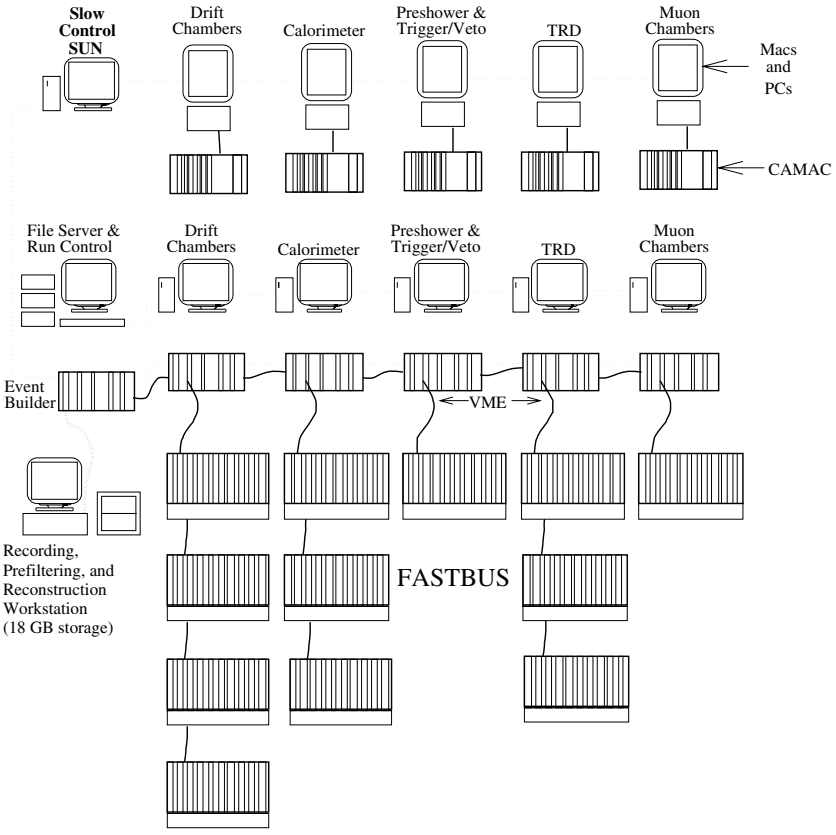

Figure 5.1: Diagram of the Data-Acquisition Hardware

into subevents, and check it for consistency and integrity. They then pass the subevents through a Vertical Inter-Crate bus (VIC) to a sixth VME processor, referred to as the "event builder," which assembles all the pieces into complete events together with information about the beam extraction and writes them to one of two nine gigabyte disks via TCP/IP communication over a dedicated ethernet connection. Several Sun Sparc workstations monitor the quality of the data and the status of the detectors.

5.3 Software

The data-acquisition software centers around elements known as *stages*. These stages use the CERN-designed CASCADE software which provides a well-organized framework for DAQ development including scheduling, buffer management and event access facilities. The arrival of data drives the stages; hence, stages must have at least one input source along with any number of output sources. The standard configuration for NOMAD is shown in figure 5.2. The event-builder stage also asynchronously receives beam calibration data, summaries of monitoring information, and detector status information whenever they change.

The slow control system consists of a Sun workstation and several Apple Macintosh computers running LabView graphical software. These computers

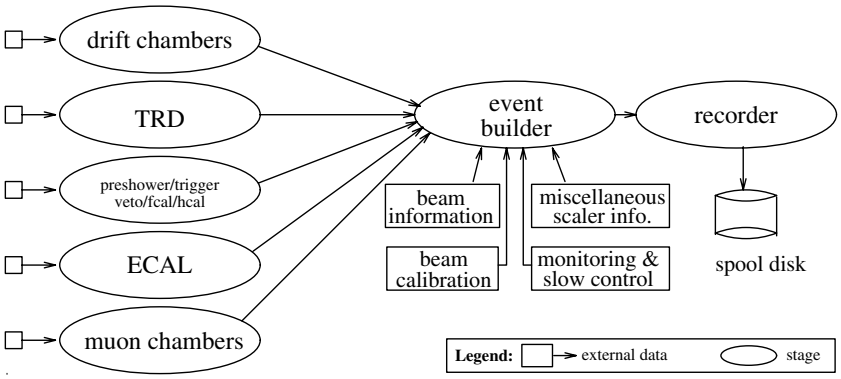

Figure 5.2: Data-acquisition Software Configuration

monitor all high and low voltages, gas systems, and temperatures in the experiment passing all data to the Sun workstation, which generates alarms when needed. In the event of a detector failure, the event-builder stage receives the alarm information which it saves for offline use.

Monitoring programs for each of the nine subdetectors as well as for beam, scaler and trigger information connect to the stages via ethernet and generate summary histograms. Shift personnel use the resulting histograms to verify the quality of the data. Additionally, a separate monitoring task reconstructs all the muon events received during the flat-top of each SPS cycle and records them in a separate data stream.

The run-control (NRC) consists of a Finite-State Machine (FSM) implemented in C++ with an X-windows interface. It uses a database both to record the current state of all the stages and monitoring programs and to determine

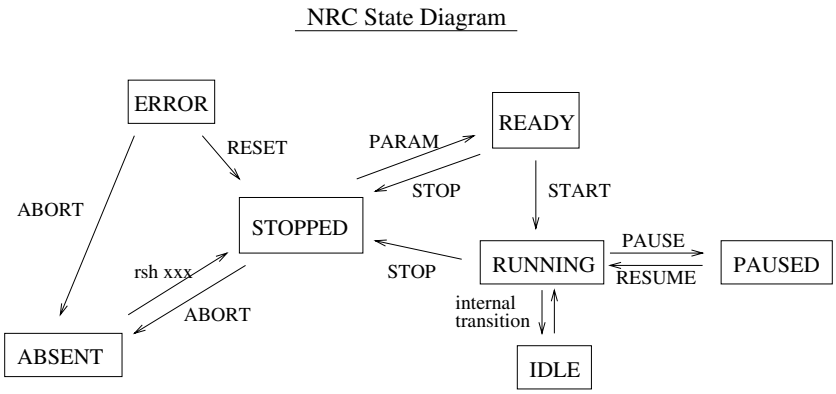

FSM hierarchy, available states, and transitions and associated commands are all loaded from a database (based on the ORACLE system).

Figure 5.3: The States of the NOMAD Run Control

rules for transitions between the various states. Figure 5.3 shows the states and transitions. Periodically, the offline software retrieves summary information for completed runs from this database and combines them with tape information for use during reconstruction and analysis. The system records over 1.5 megabytes of data per minute, with a typical assembled neutrino event containing around 2000 32-bit words before reconstruction. Additionally, approximately six times this quantity flows through the acquisition in the form of calibration events which are not recorded. In the neutrino spills, the data-acquisition has a typical deadtime of 10% arising from digitization. The data-taking time lost due to down-time and inter-run transitions is less than 3%.

Chapter 6

Monte Carlo Simulation

The inside of a typical high-energy particle physics detector during an interesting physics event is normally quite complicated. The intricacies of the beam, the detector geometry, the physics processes, etc. can fool the intuition of even the most experienced physicist. In this environment, proper simulation of all these elements is crucial for one to be able to interpret the physics implications of the data obtained by the experiment.

NOMAD Monte Carlo simulation is divided into three distinct programs:

1. the neutrino beam Monte Carlo — NUBEAM,

2. the event generator — NEGLIB, and

3. the simulation of the event in the detector — GENOM.

In addition, a small, separate Monte Carlo program was used to simulate the propagation of the hypothetical $\mathcal{X}^0$ particle along the beamline.

6.1 NOMAD Monte Carlo Packages

The NUBEAM program simulates the neutrino beam line from the proton target to NOMAD. It consists of about 10,000 lines of FORTRAN code which simulate the target, the resulting secondaries, the geometry and physical effects of material along the beam line, etc... in order to determine what the flux of neutrinos through NOMAD should be including their spatial and energy distributions. The simulation performs this for ν_μ, $\overline{\nu_\mu}$, ν_e, and $\overline{\nu_e}$. A plot showing showing the muon momentum spectrum for 1995 data and Monte Carlo which takes NUBEAM as input is shown in figure 6.1.

For this analysis, one has, as input data, the number of protons on target (POT) for the data sample. However, the resulting neutrino flux comes not only from π^+ decays but also from the decays of K^+ and other particles. Since the hypothesis of this analysis is that the $\mathcal{X}^0$ is generated in a rare π^+ decay, what is pertinent here is the spectrum for π^+ coming from these protons. The spectrum for ν_μ coming from π^+ decay in the decay tunnel is shown in figure 6.2. From this plot, one can make a plot of the energy spectrum of the π^+ which generate neutrinos in NOMAD. From that one can calculate the

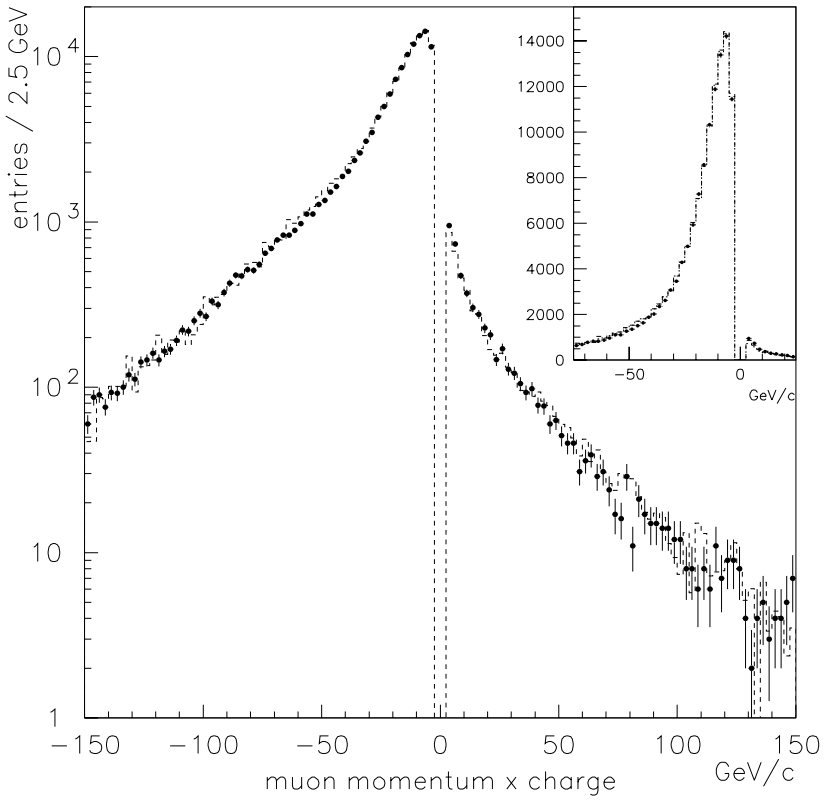

Figure 6.1: Spectrum of Muon Momenta for 1995 Data (dots) vs. Monte-Carlo (dashes) Showing Good Agreement

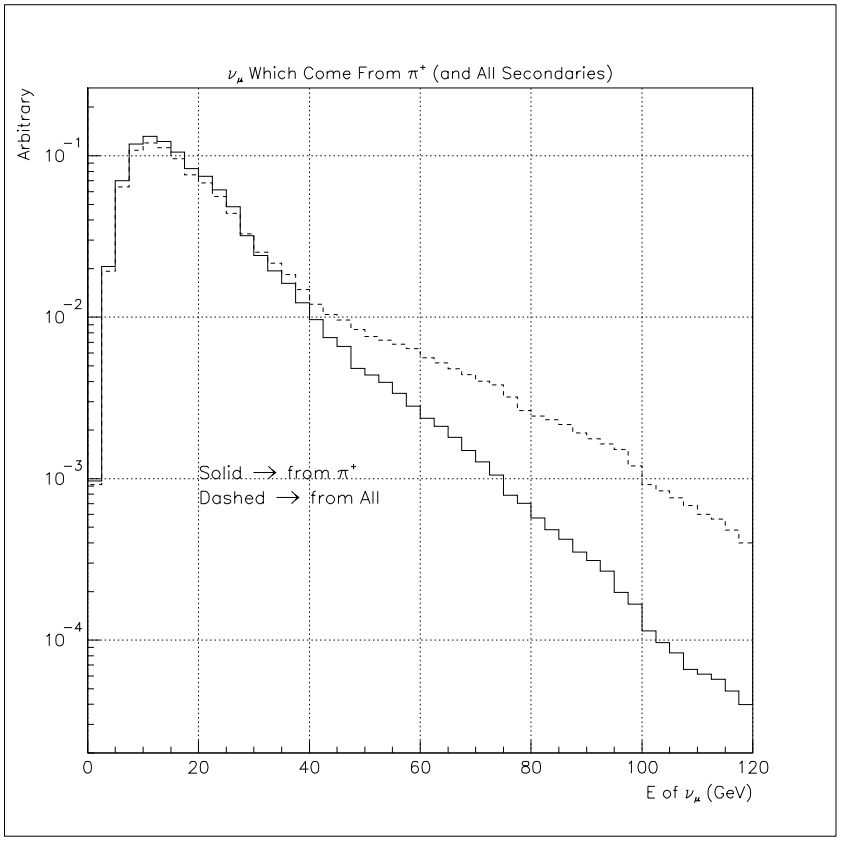

Figure 6.2: A Semi-log Plot Showing the Distribution of ν_μ and the Parent Particle Which Produced It (π^+ vs. Everything). K^+, which represent most of the difference in the two spectra, produce more ν_μ at higher energies.

difference in energies and acceptances when one substitutes $\pi^+ \to \mu^+ + \mathcal{X}^0$ for $\pi^+ \to \mu^+ + \nu_\mu$.

The NOMAD Event Generator LIBrary (NEGLIB), generates events inside the NOMAD detector itself at the level of neutrino interactions. The input comes from a modified version of LEPTO 6.1 which simulates deep-inelastic lepton-nucleon scattering[23], and from the output of the NUBEAM simulation. With this package one may choose such things as neutrino type, the beam energy window, the detector part to be used as the target for neutrino interactions, etc.... [24]. Detector geometry information is used to place vertices for interactions according to their mass distribution along the beam axis. Fermi motion of the target nucleus is also simulated. This package saves the information taken from the LEPTO package as well as NOMAD-specific information as output.

The GENOM (GÉant NOMad) package[25], uses the CERN-designed GÉANT package[26] which is a general package for simulating the passage of particles through matter including most physics interactions. GENOM describes all the pieces of the NOMAD detector. As input to the simulation, one can choose:

- events output by the NEGLIB package,
- "test beam" mode where single particles of some type are simulated with

a flat energy distribution, or

- cosmic rays.

The physics processes simulated by the GÉANT package include:

Physics Processes Handled by GÉANT				
Process	**photons**	$e^{\pm}$	$\mu^{\pm}$	**hadrons**
e^+, e^- conversion	•			
compton scattering	•			
photoelectric effect	•			
photofission of heavy elements	•			
Rayleigh effect	•			
multiple scattering		•	•	•
ionization and δ-rays		•	•	•
Bremsstrahlung		•	•	
decay in flight			•	•
positron annihilation		•		
Čerenkov radiation		•	•	
synchrotron radiation		•		
ionization by heavy ions			•	
direct e^+, e^- pair production			•	
nuclear interactions			•	
hadronic interactions				•

For this analysis, NEGLIB-simulated neutrino events (ν_μ, $\overline{\nu_\mu}$, ν_e) were simulated in the drift chamber, preshower lead, and ECal volumes in order to determine the effect of proposed cuts on background. These were all processed by GENOM and then by the reconstruction program.

Also a number of particle types were put through the detector in GENOM's test beam mode using different initial vertex regions and energy ranges. Naturally, this includes photons.

6.2 The KARMEN Particle Simulation

For this analysis, a short program was written to simulate $\pi^+ \rightarrow \mu^+ + \mathcal{X}^0$ in the NOMAD beamline. The program takes three variables from appropriate distributions as input:

- the lifetime of the $\mathcal{X}^0$ chosen from a uniform distribution,
- the energy for a ν_μ chosen from the spectrum of those coming from π^+, and
- the decay point of the π^+ chosen from an exponential distribution.

With these numbers, one can calculate the energy of the average π^+ which would generate this ν_μ. The fraction of π^+ which survive (in vacuum) until time t is given by:

$$P_{survive} = e^{\frac{-t/\tau}{\gamma}}$$

where γ is the well-known factor $\gamma = (1-\beta^2)^{-1}$. This can be used to determine whether a given π^+ decays inside the decay tunnel. For purposes of simulation, those which do decay can all be assumed to decay via:

$$\pi^+ \rightarrow \mu^+ + \mathcal{X}^0$$

and then the probability for this particle to decay between the beginning of the NOMAD drift chambers and the preshower lead can be assessed and weighted

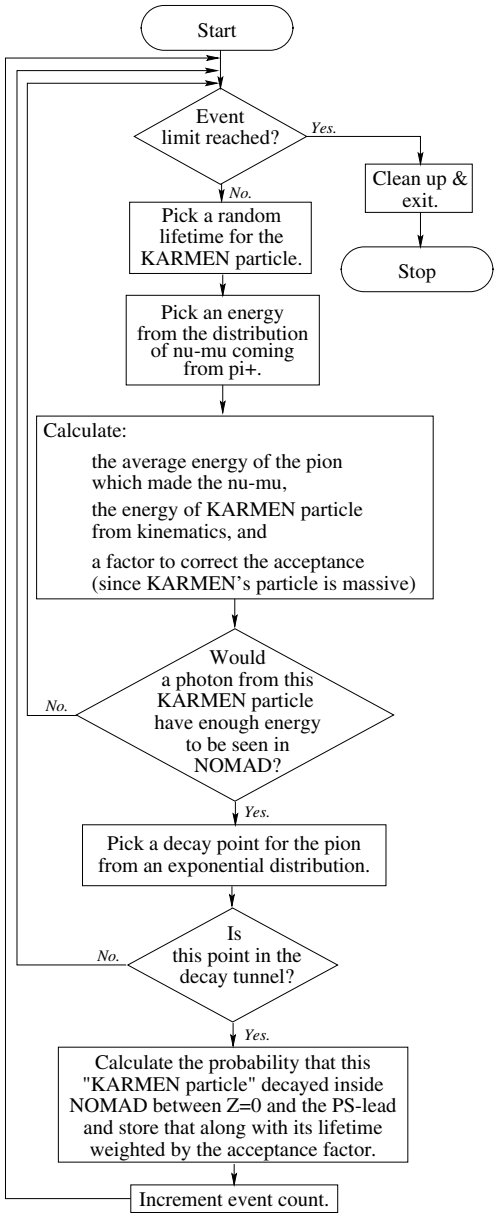

Figure 6.3: Flow diagram for the KARMEN Particle ($\mathcal{X}^0$) Simulation

according to the difference in acceptance for $\mathcal{X}^0$ versus ν_μ. The flow diagram for this program is shown in figure 6.3. The resulting output can be used to determine NOMAD's sensitivity to such decays as a function of the lifetime of the $\mathcal{X}^0$. Combining this with the ν_μ flux for the data sample and assuming some branching ratio for $\mathcal{X}^0 \to \nu + \gamma$, one can determine how many events should be seen in NOMAD. This information will be used in chapter 8 to set a limit on the abundance of this rare π^+ decay mode.

Chapter 7

Data Reduction

The pursuit of increasingly accurate measurements of physical phenomena, combined with rapid advances in electronics and computing power, are making experiments which require little or no compaction of the data more of a rarity. In 1995, the NOMAD experiment wrote approximately twenty-six million triggers on almost 2000 IBM^{TM} 3480 tapes. Since each of these tapes needs to be mounted by a human operator and since most physics analyses require repeated passes through the data, data reduction is essential in the context of NOMAD.

Using a simple program, I have filtered all the 1995 data. Selecting only $\overline{(T_1 T_2)} ECal$ and $\overline{V_{wide}} ECal$ triggers and applying a few very loose criteria, the data sample has been reduced to approximately 200,000 events. The choice

of criteria will become apparent in chapter 8. A flow diagram of the filter program is shown in figure 7.1. The resulting output constitutes twenty-seven files of less than 200 megabytes each, all of which fit quite easily onto one high-density DLT tape with a ten gigabyte capacity. This tape is kept in a tape "robot" where it is quickly mounted when needed.

While a reduction in data by a factor of more than 10^2 is obtained with this filter, a further level of data reduction is desirable. A large fraction of the data from each filtered event is not actually needed for most of the analysis; additionally, the sequential-access record format used for tape storage greatly slows down access to the data. A simple solution to this is to create direct-access, disk-based files including only those variables that one anticipates using in the analysis. Assuming that the variables are chosen intelligently enough, one can avoid frequent regeneration of the disk files. Also, small numbers of anomalous events requiring special consideration can be treated separately or "scanned" with an event-display program. Monte Carlo simulated events also fit into this scheme. It is also enlightening to see the different amount of time needed to access the data at the three different levels:

Level	Storage, Record Format	Time to Access All Events
"raw" data on tape	sequential, fixed-length	$>$ two weeks
filtered data on tape	sequential, fixed-length	$<$ 8 hours
disk files	direct-access, variable-length	$<$ 5 minutes

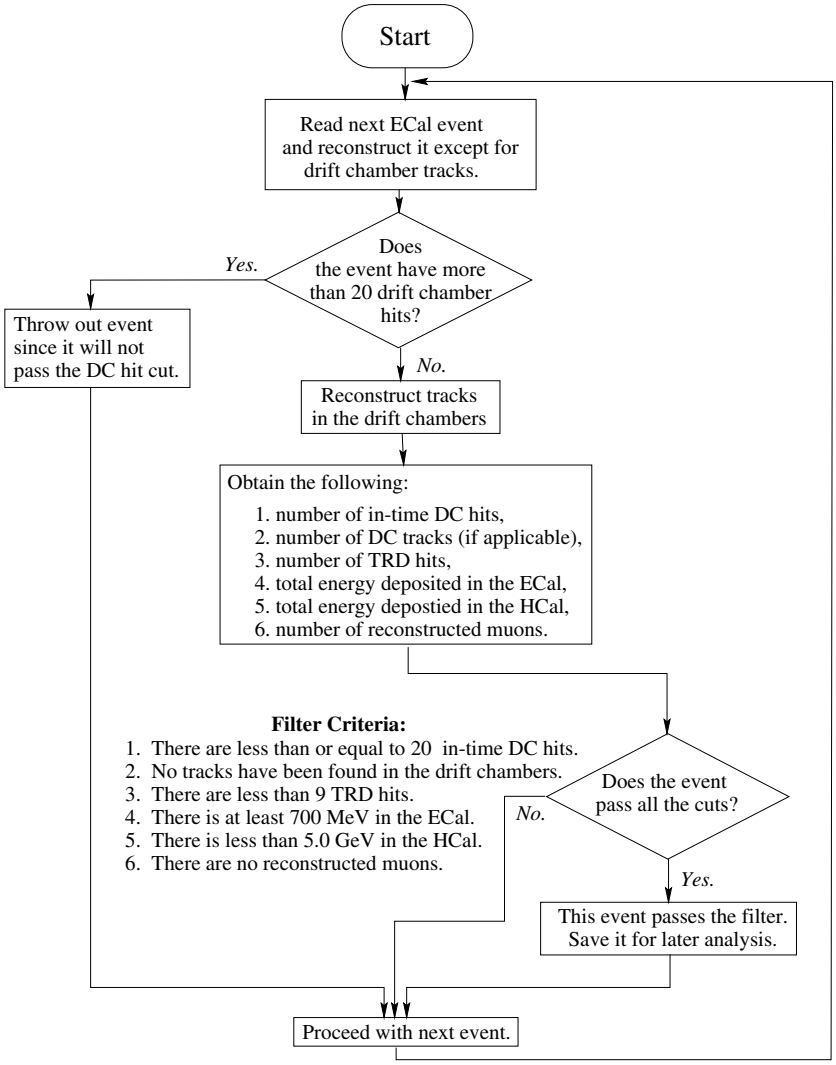

Figure 7.1: Flow Diagram of the Filter Program

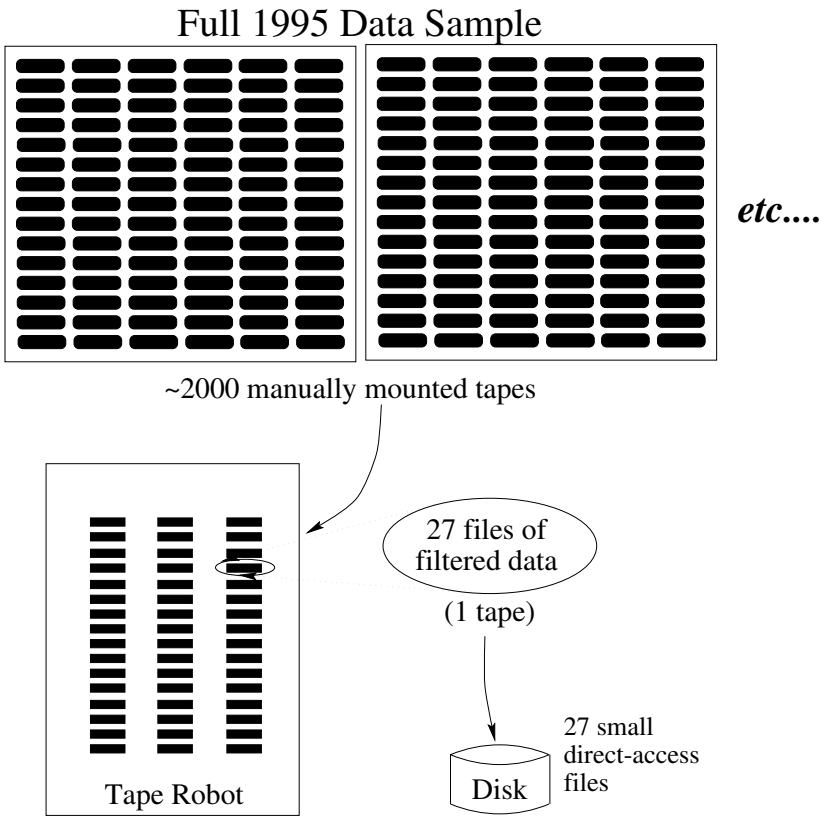

Figure 7.2: The Various Levels of Data Handling

For my analysis, one pass has been required at the raw data in order to generate the filtered sample as well as two passes at the filtered data to generate the disk files. The final format of the disk files is described in the following table:

- run number
- event number
- number of drift chamber hits
- number of drift chamber tracks
- number of TRD hits
- number of TRD tracks
- number of hits in the first trigger scintillator
- number of hits in the second trigger scintillator
- number of preshower hits in the horizontal tubes

  For every horizontal preshower tube which was hit:
  - energy deposited
  - Y location
- number of preshower hits in the vertical tubes

  For every vertical preshower tube which was hit:
  - energy deposited
  - X location
- total energy deposited in the ECal
- number of clusters reconstructed in the ECal

  For every ECal cluster:
  - total energy in the cluster
  - energy in the "center"
  - cluster classification

  - shower shape variable 1
  - shower shape variable 2
  - row number for cluster center
  - column number for cluster center
  - noise index (not used)
  - X value of cluster centroid
  - Y value of cluster centroid
- total energy deposited in the HCal
- the number of HCal slabs which were hit

  For every HCal slab:
  - central Y value for this slab
  - energy in the slab
- momentum of first muon (not used)
- number of muon hits
- number of reconstructed muon tracks

The more complicated variables are explained in the chapter on analysis. The above list of variables sufficed for almost all the analysis performed. It was necessary to scan the remaining signal events to eliminate a few events that were clearly not signal events but had managed to pass the cuts. Additionally, less than 100 additional events were scanned in order to determine certain systematic errors.

Chapter 8

The Search

With the data reduced to a manageable size and format, one can proceed with the task of searching for

$$\mathcal{X}^0 \rightarrow \nu + \gamma$$

coming from the decay

$$\pi^+ \rightarrow \mu^+ + \mathcal{X}^0$$

inside the decay tunnel. Throughout this chapter, a branching ratio of 100% is assumed for single photon decay of the $\mathcal{X}^0$.

8.1 Feasibility

With a search-type analysis, loss of efficiency for the sake of reduced background is generally acceptable. It may also be advisable to eliminate certain

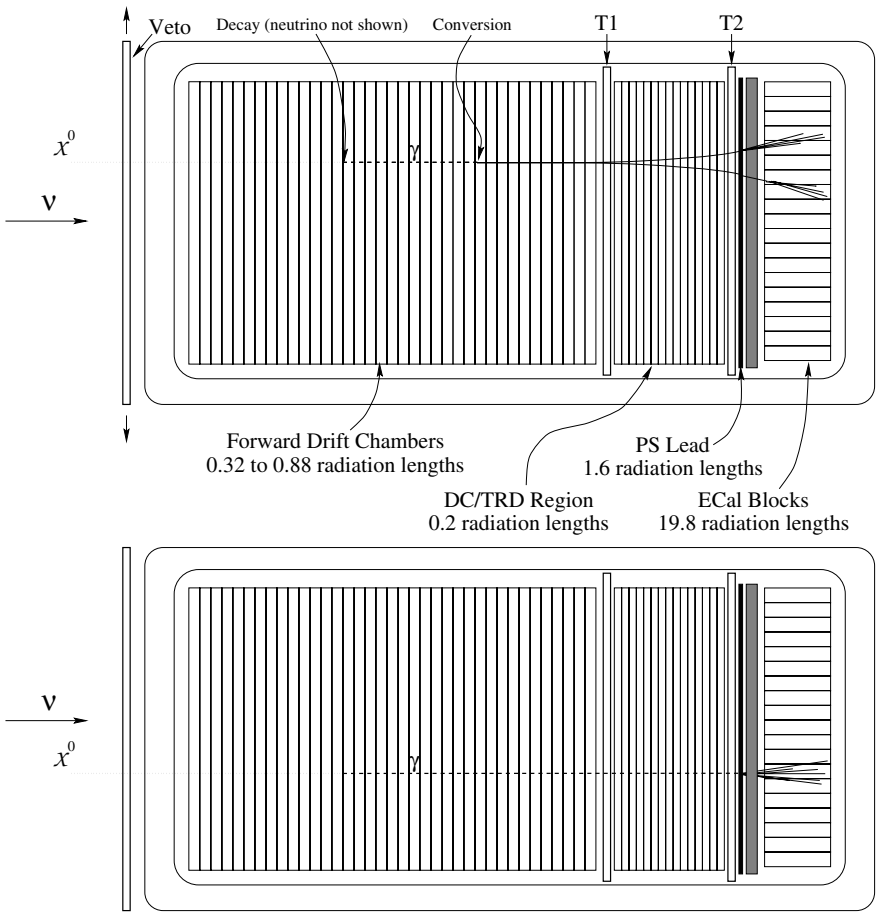

Figure 8.1: Two Drawings of Possible γ from $\mathcal{X}^0$ Decays

classes of data because of large or unknown systematic errors at the expense of statistics. First, I address the issue of how to look for photons in NOMAD. Figure 8.1 shows two examples of photon detection as well as the number of radiation lengths associated with various sections of the detector. One can perform either of the following:

1. Look in the preshower and ECal for the appropriate energy deposition

and shower shape, or

2. attempt to reconstruct photon conversions in the tracking region.

Photons from the decay of a 33.9 MeV $\mathcal{X}^0$ will be at very low angle with respect to the beam axis due to the Lorentz boost of the $\mathcal{X}^0$ in the lab frame; the signature of such photons in the ECal should be well-defined and "clean," relying mostly on shower shape for identification. By contrast, identification of photon conversions in the tracking region requires detailed understanding of the efficiency for identifying, reconstructing and vertexing $e^-(e^+)$ at various points in the detector; in addition, the systematic errors associated with reconstructing conversions are certainly much higher than those for photon identification in the preshower/ECal region. The issue of the reconstruction efficiency for conversions becomes even more involved when one considers the different quantity of chambers installed for various periods during 1995. Due to all the complicated aspects of using photons which convert in the tracking region, I have chosen to consider only those in which the photon interacts in the preshower or ECal. For similar reasons, I do not search for direct decay of the $\mathcal{X}^0$ via $\mathcal{X}^0 \to e^+e^-\nu$.

The philosophy thus becomes the following. Assuming that we expect a photon from a $\mathcal{X}^0$ decay to "appear" at some point inside the detector but before the preshower lead, any significant activity in the detectors before the

lead would indicate the presence of other physics activity in the event, such as a neutrino interaction in the target or an early conversion of the photon. These events should clearly be eliminated. Photons in the energy range of the neutrino beam which do manage to convert in the preshower or the ECal should deposit all of their energy there; i.e. the longitudinal progression of the event will stop at the ECal. Significant activity in the succeeding detectors is also an indicator that the event is not a photon. Criteria can then be applied to eliminate the primary background which should be various types of neutrino interactions in the preshower lead and the ECal. One can then look at the resulting events, some of which will have preshower hits in front of a photon-like ECal cluster, in order to obtain a measure of the abundance of the decay $\pi^+ \to \mu^+ + \mathcal{X}^0$ along the beamline.

The cuts which follow from this decision fall into three classes:

- cuts to eliminate physics processes before the preshower — the upstream region,
- those designed to select isolated photons in the ECal, and
- cuts on downstream detectors to eliminate most of the neutrino interactions coming from the preshower lead and the ECal lead-glass.

These cuts are detailed in the following sections.

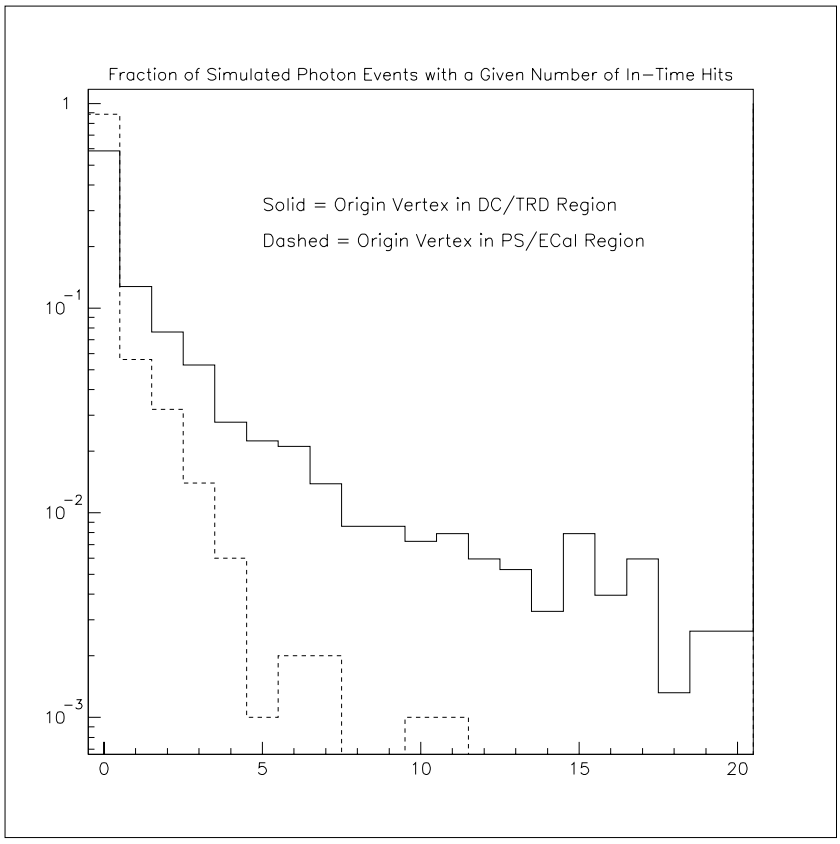

Figure 8.2: Normalized Drift Chamber Hit Count Distribution from a Small Simulation with 11 DC Modules Installed

8.2 Upstream Sub-detectors

As shown in figure 8.2, the number of drift chamber hits for photons simulated in the region between the preshower lead and the mid-point (in depth) of the ECal blocks is generally zero except for contributions from the occasional backward-going particle. Noise in the chambers, being difficult to parametrize, is not included in the simulation but generally contributes no more than a few

hits per event. Requiring less than ten hits turns out to be the tightest cut one can apply at the hit level without significantly hurting efficiency. In addition, applying this cut eliminates the need for other cuts at the drift chamber level such as cuts against reconstructed tracks, since the reconstruction software requires a minimum of ten in-time hits to reconstruct a track.

Since the TRD is interspersed with the last five drift chambers, one might find it somewhat less necessary to consider activity here after having applied the drift chamber cuts. The TRD is also more free of noise than the drift chambers but is still subject to "back-splash" from the preshower as with the drift chambers. In the interests of keeping the signal events as "clean" as possible, I cut out all events with more that two hits in the TRD straw chambers. This cut has an efficiency of 96% after previous cuts.

Due to the level of effectiveness of these cuts, it was not necessary to use the trigger scintillators or the FCal information to eliminate events.

8.3 Downstream Sub-detectors

Whatever happen in the preshower, the ECal and upstream detectors, photons of any energy should not leave significant traces in the downstream detectors. The filter pass on the data has already rejected events with reconstructed muons, (see figure 7.1). However, there is a large number of muons coming

from neutrino interactions in the ECal and some muons may either range-out in the iron wall between the two muon stations, or may be lost due to multiple scattering. So it is advisable to put additional cuts. Keeping only events with less than 3 hits in the muon chambers tightens the criteria while maintaining an efficiency of 99.9% after the previous cuts.

The HCal is immediately downstream of the ECal in the magnet return yoke (see figure 4.1). Not only does it provide a reasonable indicator of the presence of hadronic activity, but its proximity to the ECal allows it to make a complimentary check against muons. Of all the sub-detectors, however, it does have the feature of being the noisiest. Thus, cuts on the HCal must be looser and the systematic errors associated with it are higher. In order not to hurt efficiency too much, two separate cuts have been used:

- a cut requiring less than 300 MeV of energy deposition in the HCal and
- a cut which throws out events with more than three hit HCal slabs.

The efficiency of the two cuts together is 82.6% after previous cuts.

8.4 Electromagnetic Calorimeter

The center-point of the analysis comes at the level of the ECal. After the previous cuts, all the subdetectors except the preshower and the ECal are

quiescent. Photon identification can then be made based upon several criteria involving groups of cells, or *clusters* :

- the number of clusters — i.e. exactly one,
- the total energy deposition, and
- the shape of the cluster in order to reject:
  - particles which are not photons and
  - clusters due to noisy channels.

Requiring a single cluster is clearly necessary, since multiple clusters indicate an early conversion of the photon, event overlap, or some other activity. Eliminating such isolated photons reduces the efficiency to 88.8% with respect to that left after previous cuts.

At the same time, a minimum energy requirement in the ECal enables one to eliminate muons which deposit energy in the ECal in the form of Čerenkov radiation. The spectrum for muons in the ECal was shown in figure 4.5. The spectrum peaks at 500 MeV but has a tail extending past 1 GeV. To eliminate this as well as some noise, events which have less than 1.5 GeV are rejected.

For each cluster which remains one must be able to define a "center" in order to determine the profile of the cluster. A naïve choice would be to take the cell with the largest energy deposition. This, however, results in a

granularity in the central location of the order of the dimensions of a block, i.e. a few centimeters. While trying such a scheme during early tests, I also discovered that individual blocks could be quite noisy and would generate fictitious events, albeit quite infrequently. To make matters more complicated, these events were distributed rather uniformly over the detector, appearing only for brief periods. Thus, mapping these for all of the 1995 run would have been rather difficult. The Molière radius, R_M, which characterizes the transverse development of showers, is on the order of the transverse dimensions of the block. Since photons strike random parts of a block, they almost always deposit a significant amount of energy in some other cell besides the highest energy cell.

In order to deal with these two problems, I developed a simple classification system for clusters. This is depicted in figure 8.3. The classification scheme separates clusters according to how many blocks have energy deposition above 1 GeV, thus defining the "center," and whether there are any blocks adjacent to these with energy deposition of at least 100 MeV. The central cells, themselves, only include those cells with at least 1 GeV energy deposition. Events whose cluster is of the *NO_CENTER* class, are not suitable for shower shape cuts and are thus discarded. Events with clusters of the *CENTER_1_ALONE* variety, with a single block with more than 1 GeV but no other adjacent blocks above

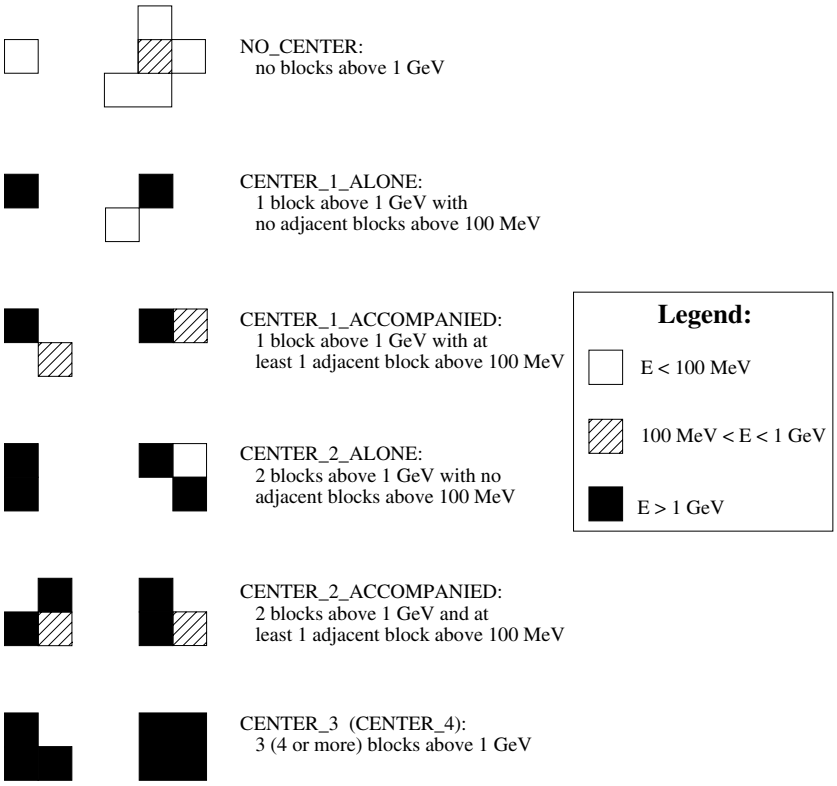

Figure 8.3: Cluster Classes with Examples: The first two are excluded

100 MeV, are very rarely photons ($< 4\%$) but rather due to noisy channels. These events are also discarded. All other classes are kept.

In order to be able to make cuts based on shower shape, the transverse development of the shower must be contained in the ECal. So, after previous cuts requiring a well-defined center for the cluster; that center is required to lie inside a region defined by:

$$-120 \text{ cm} < X_{center} < 120 \text{ cm}$$

$$-120 \text{ cm} < Y_{center} < 120 \text{ cm}$$

Although this reduces the fiducial region to 64% of its full size, the shape of the beam is such that only about 10% of the neutrino flux is lost.

Finally, photons entering the ECal along the beam axis will generate a very narrow shower when compared to $\pi^{\pm}$ or that expected from ν_e-CC interactions. In order to measure this shape two variables are defined:

$$R_1 = \frac{\sum_{i=1}^{N_{center}} E_i}{\sum_{i=1}^{N_{center}} E_i + \sum_{i=1}^{N_{radius=1}} E_i}$$

$$R_2 = \frac{\sum_{i=1}^{N_{center}} E_i}{\sum_{i=1}^{N_{center}} E_i + \sum_{i=1}^{N_{radius=2}} E_i}$$

where *radius=1* and *radius=2* refer to cells touching the central cells and cells touching those which touch the central cells, respectively. These two variables range between zero and one, with larger values indicating more narrow showers. Figure 8.4 shows the spectrum for photons (solid), ν_μ neutral current (dashed), and ν_e charged current (dotted) Monte-Carlo events which survive all the previous cuts. Note that each sample is normalized to one and in both cases the peaks for photons are the most biased toward one. After many adjustments of these cuts, they were finally set to require:

$$R_1 > 0.9$$

$$R_2 > 0.96$$

This cut being the final cut before scanning, I present a summary of the cuts, the number of events they leave and the efficiency for keeping photons which have not interacted before the preshower lead.

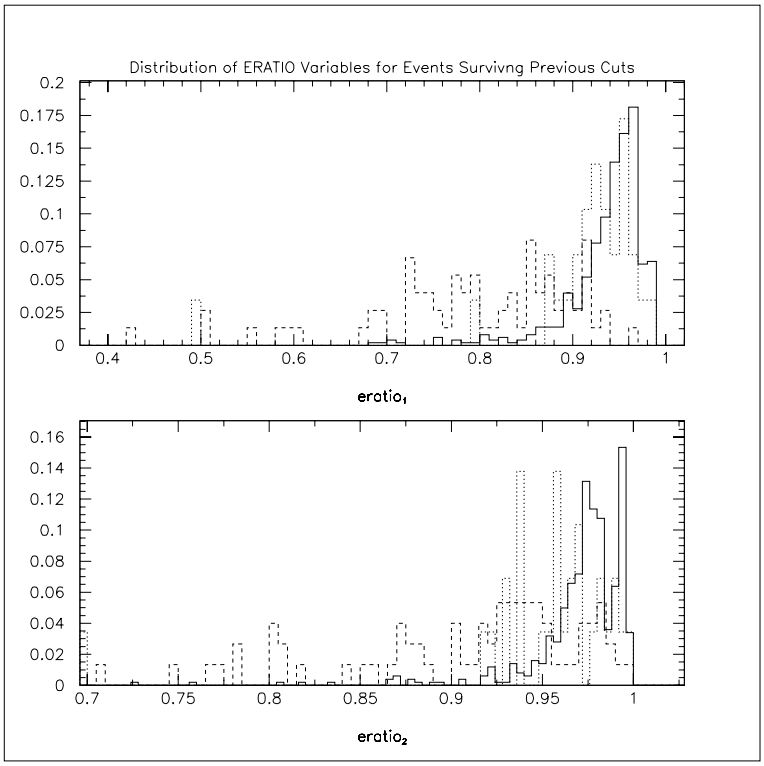

Figure 8.4: Spectrum of the R_1 and R_2 Variables. The solid lines are for photons.

Cuts and and Their Effects on Data and Monte-Carlo		
Cut	**Data Events Remaining**	ϵ_{mc} **for** γ
(Filter Cuts)	198,802	97.8 %
$N_{DCHits} < 10$	178,066	97.8 %
$N_{TRDHits} < 3$	166,540	97.4 %
$N_{MuonHits} < 3$	65,407	97.1 %
$E_{HCal} < 300$ MeV	46,172	91.7 %
$N_{HCalHits} < 4$	44,957	91.7 %
$N_{ECalClusters} = 1$	11,323	80.0 %
$E_{ECal} > 1.5$ GeV	2,547	(required)
$Class_{Cluster}$ requirement	1,262	77.4 %
$Center_{Cluster}$ inside $\pm$120cm	941	(required)
$R_1 > 0.9$	148	66.4 %
$R_2 > 0.96$	98	59.7 %

Three events from the 1995 data were eliminated in subsequent scanning. These events were pathological cosmics which slipped through the other cuts.

8.5 Preshower

As there are only ninety-five events after all cuts in the 1995 data. Analysis of the preshower content of these events has been done by hand scanning. Events are associated to the preshower when there is energy deposition of at least 1 MIP in one or more tubes in front of the center or up to one cell width from

the center of the cluster. Seven events of the 95 meet this criteria. A display of the preshower and the calorimeter for one of these events is shown in figure 8.5 as well as a "lego" plot of the energy deposition in the calorimeter with the energy threshold for display turned off in figure 8.6. The energy distribution of all the candidate events is shown in figure 8.7 and their cluster classifications are shown in figure 8.8.

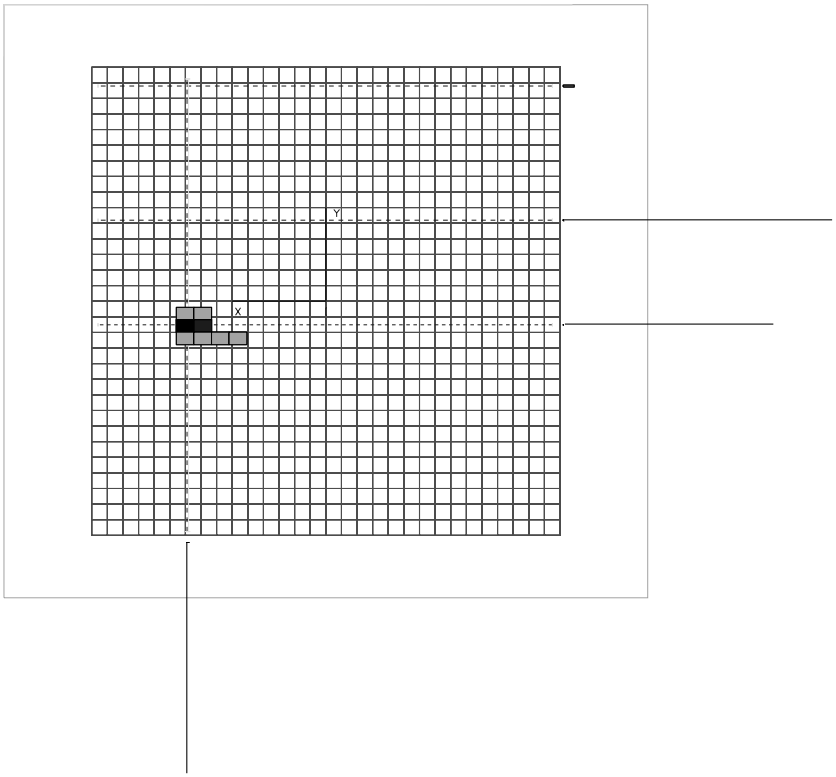

Figure 8.5: A Photon Candidate Showing both Preshower and ECal Activity. The shaded blocks represent ECal blocks with the darker colors indicating higher energy deposition. The protruding lines indicate the amount of ionization resulting from the passage of particles through a given horizontal or vertical preshower tube. (Run 9333, Event 16686)

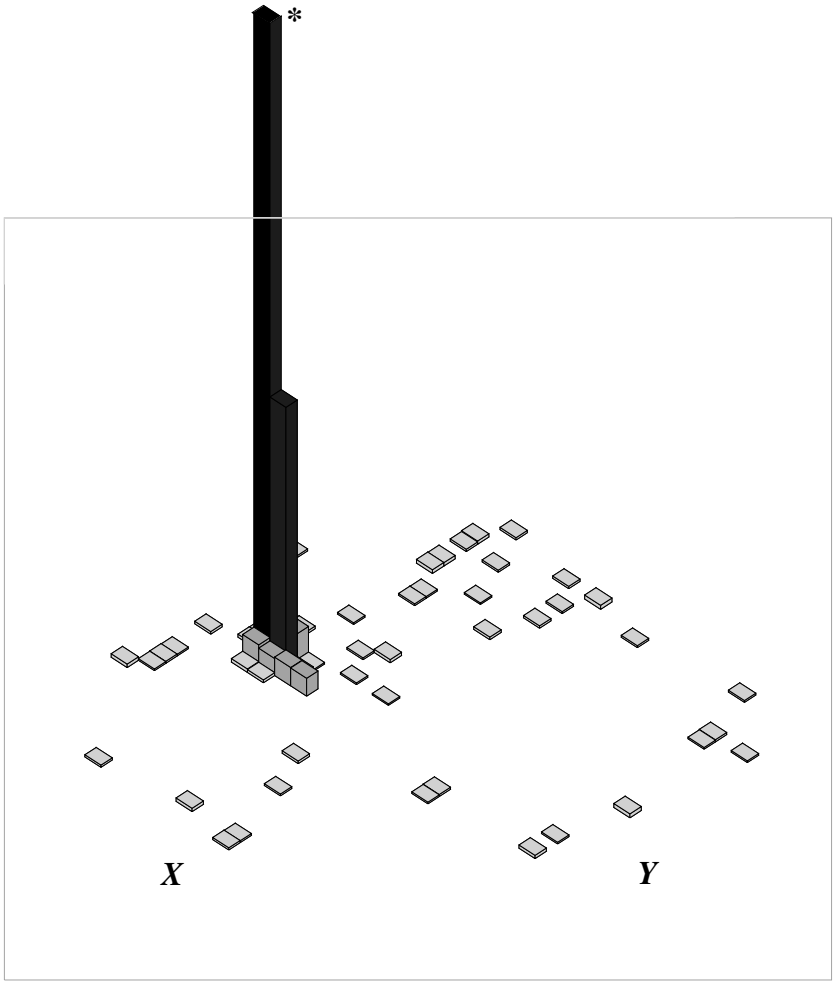

Figure 8.6: An ECal "Lego" Plot Showing the Structure of the Energy Deposition in the ECal for the Same Candidate Event (Run 9333, Event 16686).

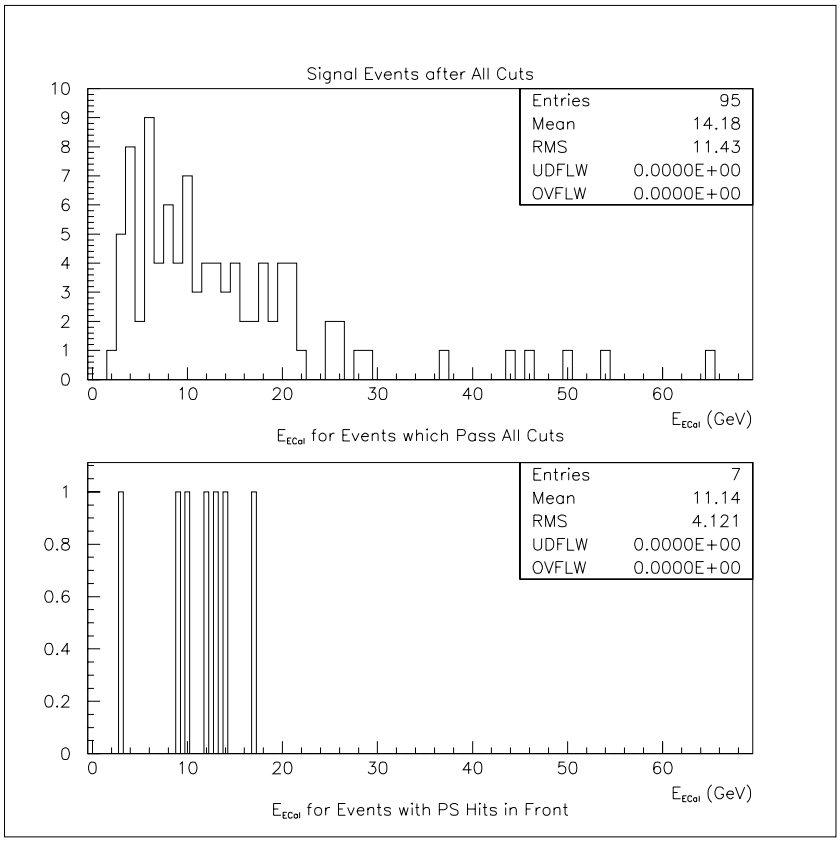

Figure 8.7: E_{ECal} for All Events Which Pass the Cuts and Then for Those Which Have Preshower Hits in Front

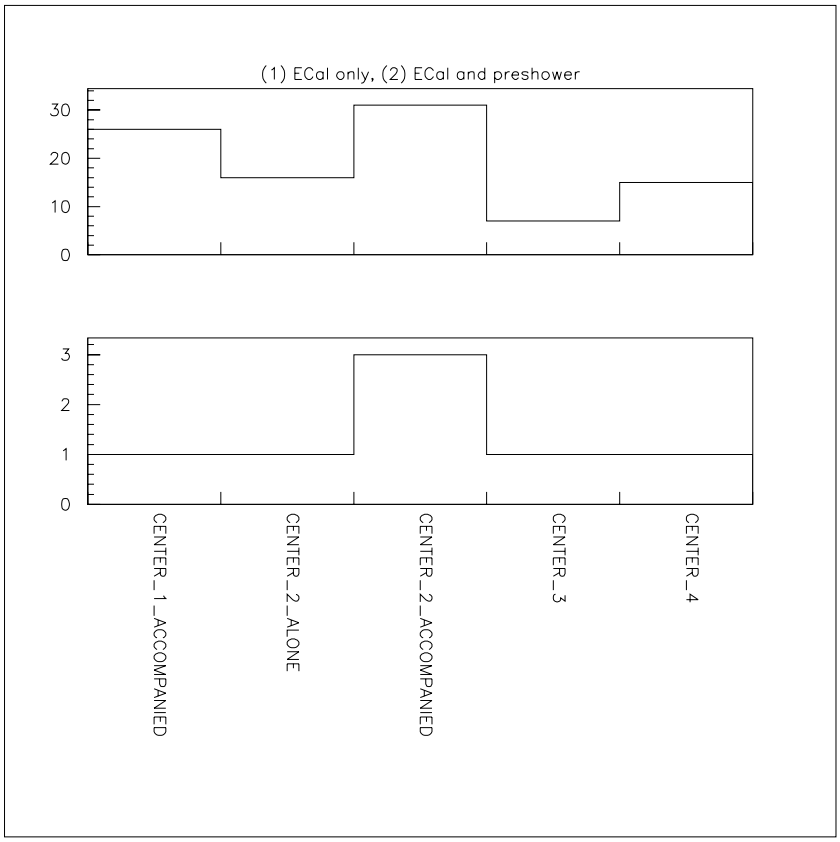

Figure 8.8: The ECal Cluster Class for the Events Passing All Cuts and Then for Those with Preshower Hits in Front

Thus one obtains the value $\boxed{0.074 \pm 0.027 \text{ (statistical)}}$ for the ratio of events which have both preshower and ECal activity normalized to all those which have ECal activity. The theoretical value expected from neutrino interactions in the preshower/ECal region is given by:

$$\frac{active\ mass\ in\ preshower}{active\ mass\ in\ ECal} = 0.084$$

The only thing lacking are systematic errors on this ratio which have been obtained by varying the cuts slightly. The table below summarizes them:

Systematic Errors for Various Cuts	
Cut	**Error on the Ratio**
N_{DcHits}	0.007
$N_{TRDHits}$	0.007
$N_{MuonHits}$	0.009
E_{HCal}	0.013
$N_{HCalHits}$	0.015
R_1	0.007
R_2	0.004
cluster classes	0.006

All errors are taken as uncorrelated except the (R_1, R_2) cuts which are assumed to be fully correlated. This gives an overall systematic error of 0.027. So from data, one obtains:

$$\frac{N_{Preshower+ECal}}{N_{ECal}} = 0.074\ \pm 0.027\ (systematic)\ \pm 0.027\ (statistical)$$

with theory predicting 0.084. Photons from the decay of a $\mathcal{X}^0$ inside NOMAD would increase this ratio (0.074) for the data. Whether or not this increase would be significant depends upon an extensive simulation of the Monte-Carlo

processes which could manifest themselves in the data given the cuts used. This has not been done. Nevertheless, the events which remain are completely consistent with those expected from physics processes like:

- ν_e quasielastic interactions,
- neutral current interactions which generate multiple π^0, and
- coherent-π^0.

Hence, there is no clear evidence for the $\mathcal{X}^0$ at this level.

One can, however, take a more conservative approach. Given the efficiency for detecting photons and the number of events observed in the preshower, one can assume that **all** the events in the preshower are from decays of $\mathcal{X}^0$, and then set limits on $\Gamma(\mathcal{X}^0 \to \nu + \gamma)$ as a function of the lifetime of the $\mathcal{X}^0$ as was described in Chapter 6.

Of the photons which appear from decays inside NOMAD, Monte-Carlo predicts that 69.7% should reach the preshower lead without converting in the drift chamber region. Of those which remain, 71.1% should convert in the preshower lead. Of those, 59.7% should be detected with the above cuts. Data-acquisition livetime, weighted over the trigger types, is 84%. In order to get a 90% confidence-level upper-limit, we also need to multiply by 1.28.

Combining these factors, the number of events in NOMAD is less than:

$$\frac{7 \text{ events} \times 1.28}{0.697 \times 0.711 \times 0.597 \times 0.84} < 35.9 \text{ events at } 90\% \text{ CL}$$

From the beam Monte-Carlo, the number of ν_μ resulting from 6.13×10^{18} protons on target which pass inside a $\pm 120cm \times \pm 120cm$ area is $\boxed{7.0 \times 10^{16} \nu_\mu.}$ One can then take the number of events excluded at 90% confidence level and divide by the flux of ν_μ, obtaining 5.13×10^{-16}. From chapter 6, we know the probability, P_{decay}, for a given $\mathcal{X}^0$ lifetime, that it will decay to a photon inside NOMAD, including adjustments to the flux and energy coming from the different kinematics for π^+ decay to the massive $\mathcal{X}^0$ instead of decay to ν_μ. The ratio, $\frac{5.13 \times 10^{-16}}{P_{decay}}$, can be plotted versus the $\log_{10}$ of the $\mathcal{X}^0$ lifetime. This can be compared to the plot of KARMEN's sensitivity for exclusion purposes. Figure 8.9 shows the regions excluded by this analysis.

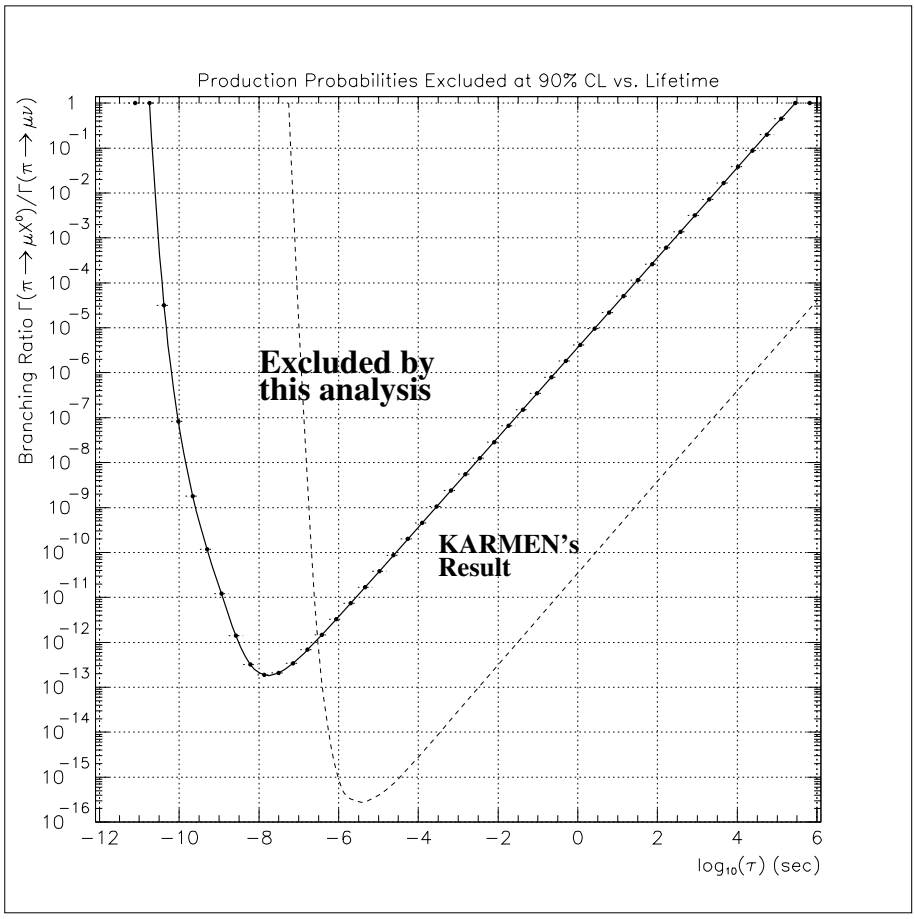

Figure 8.9: Excluded Branching Ratios vs. $\log_{10}(\tau_{\mathcal{X}^0})$

Chapter 9

Conclusion

Two types of NOMAD triggers, $\overline{V_{wide}}ECal$ and $\overline{(T_1T_2)}ECal$, were examined in 1995 data for evidence of the decay

$$\mathcal{X}^0 \to \nu_\mu + \gamma.$$

For 6.13×10^{18} protons on target, seven events pass all cuts and their relative abundance is completely consistent with that expected from normal neutrino interaction in the detector. The resulting limits are shown in figure 8.9 on page 84 and exclude branching ratios for this rare decay down to 2×10^{-13} for $\tau_{\mathcal{X}^0} \sim 10^{-8}$ s. These limits assume that the $\mathcal{X}^0$ decays exclusively to the above channel; in consideration of models where this is not the case, the limit should be scaled appropriately.

9.1 Possibilities for Improvement

This result could probably be improved by additional simulation in order to allow a reliable background subtraction to be performed. Additionally, increased statistics from the 1996 and 1997 NOMAD runs should allow an improvement of ~ 3. It is unlikely, however, that the decay volume can be expanded or that the cuts can be changed in a way which will dramatically change the results. And while this analysis represents a significant exclusion to the region of parameter space which can accommodate the KARMEN anomaly, increases in statistics alone will not be able to totally exclude the allowed regions. KARMEN, itself, plans an upgrade which will increase their signal to noise ratio substantially. Hopefully, this can shed more light upon the anomaly.

9.2 Measurements by Other Experiments

NOMAD is, by no means, the only experiment which can assess the KARMEN anomaly. Others, notably two at the Paul-Scherrer Institute [27, 28], are able to rule out other regions of parameter space. These experiments exclude certain branching ratios independently of the lifetime of the $\mathcal{X}^0$:

$$BR(\pi^+ \to \mu^+ \mathcal{X}^0) \quad < \quad 7 \times 10^{-8} \qquad (95\%\text{CL}) \quad [27]$$

$$BR(\pi^+ \to \mu^+ \mathcal{X}^0) \quad < \quad 2.6 \times 10^{-8} \quad (95\%\text{CL}) \quad [28]$$

Additional experiments are being proposed by the same groups in order to improve this number. There are others who are attempting to measure this phenomena, but they are significantly less sensitive than the NOMAD and PSI-based experiments. [29] A second figure which shows the 90% CL exclusion plot for this analysis overlaid with the region excluded by Daum *et al.* [28] is shown in figure 9.1. It is the sincere hope of the author that this "anomaly" can be decisively resolved, whether it be by confirmation or complete exclusion, in the near future.

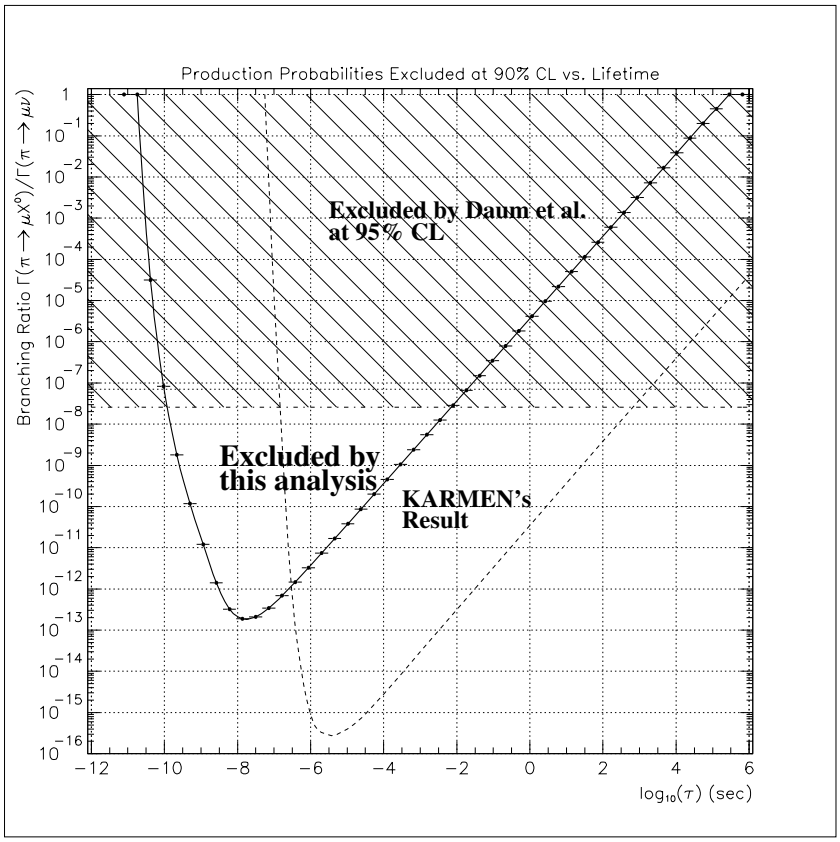

Figure 9.1: Excluded Branching Ratios vs $\log_{10}(\tau)$ with the Exclusion by Daum et al.

The NOMAD Collaboration

J. Altegoer[5] C. Angelini[17] P. Astier[15] D. Autiero[4] A. Baldisseri[19] M. Baldo-Ceolin[14] G. Ballocchi[4] M. Banner[15] S. Basa[10] G. Bassompierre[2] K. Benslama[10] I. Bird[10] B. Blumenfeld[9] F. Bobisut[14] J. Bouchez[19] S. Bunyatov[6] S. Boyd[21] A. Bueno[1,8] L. Camilleri[4] A. Cardini[11] A. Castera[15] P.W. Cattaneo[16] V. Cavasinni[17] G. Conforto[18] C. Conta[16] R. Cousins[11] A. De Santo[17] T. Del Prete[17] L. Di Lella[4] T. Dignan[8] I. Donnelly[20] J. Dumarchez[15] L. Dumps[4] T. Fazio[2] G. Feldman[8] R. Ferrari[4] D. Ferrere[4] V. Flaminio[17] M. Fraternali[16] J-M. Gaillard[2] P. Galumian[10] E. Gangler[15] A. Geiser[4] D. Geppert[5] D. Gibin[14] S. Gninenko[13] J-J. Gomez-Cadenas[1,4] J. Gosset[19] C. Gößling[5] M. Gouanere[2] A. Grant[4] G. Graziani[7] D. Kekez[22] A. Guglielmi[14] C. Hagner[19] J. Hernando[1] D. Hubbard[8] P. Hurst[8] W. Huta[4] N. Hyett[12] E. Iacopini[7] C. Joseph[10] M. Kirsanov[7] B. Khomenko[4] O. Klimov[6] A. Kovzelev[13] O. Kuznetsov[6] A. Lanza[16] L. La Rotonda[3] M. Laveder[14] C. Lazzeroni[17] A. Letessier-Selvon[15] J-M. Levy[15] L. Linssen[4] M. Livan[16] A. Ljubičić [22] J. Long[9] A. Lupi[7] E. Manola-Poggioli[2] A. Marchionni[7] F. Martelli[18] J-P. Mendiburu[2] J-P. Meyer[19] M. Mezzetto[14] S. Mishra[8] G. Moorhead[12] L. Mossuz[2] P. Nedelec[2,4] Yu. Nefedov[6] C. Nguyen-Mau[10] D. Orestano[16] F. Pastore[16] L. Peak[21] E. Pennacchio[18] J-P. Perroud[10] H. Pessard[2] R. Petti[16] A. Placci[4] H. Plothow-Besch[4] A. Pluquet[19] G. Polesello[16] D. Pollmann[5] B. Pope[4] B. Popov[6,15] C. Poulsen[12] P. Rathouit[19] G. Renzoni[17] A. Rimoldi[16] C. Roda[4] A. Rubbia[4] F. Salvatore[16] K. Schahmaneche[15] B. Schmidt[5] A. Sconza[14] M. Sevior[12] D. Sillou[2] P. Soler[21] G. Sozzi[10] D. Steele[9] D. Stefen[4] M. Steininger[10] M. Stipčević [22] T. Stolarczyk[19] G. Taylor[12] S. Tereshchenko[6] A-M. Touchard[15] S. Tovey[12] M-T. Tran[10] E. Tsesmelis[4] J. Ulrichs[21] V. Uros[15] M. Valdata-Nappi[3] S. Valuev[6,2] F. Vannucci[15] K. Varvell[20] M. Veltri[18] V. Vercesi[16] D. Verkindt[2] J-M. Vieira[10] M. Vo[19] S. Volkov[13] F. Weber[4,8] T. Weiße[5] M. Werlen[10] F. Wilson[4] P. Wicht[4] L. Winton[12] B. Yabsley[21] H. Zaccone[19]

[1]Univ. of Massachusetts, Amherst, USA
[2]LAPP, Annecy, France
[3]Univ. of Calabria and INFN, Cosenza, Italy
[4]CERN, Geneva, Switzerland
[5]Dortmund Univ., Dortmund, Germany
[6]JINR, Dubna, Russia
[7]Univ. of Florence and INFN, Florence, Italy
[8]Harvard Univ., Boston, USA
[9]Johns Hopkins Univ., Baltimore, USA
[10]University of Lausanne, Lausanne, Switzerland
[11]UCLA, Los Angeles, USA
[12]University of Melbourne, Melbourne, Australia
[13]Inst. Nucl. Research, INR Moscow, Russia
[14]Univ. of Padova and INFN, Padova, Italy
[15]LPNHE, Univ. of Paris, Paris VI and VII, France
[16]Univ. of Pavia and INFN, Pavia, Italy
[17]Univ. of Pisa and INFN, Pisa, Italy
[18]Univ. of Urbino, Urbino, and INFN Florence, Italy
[19]DAPNIA, CE Saclay, France
[20]ANSTO Sydney, Menai, Australia
[21]University of Sydney, Sydney, Australia
[22]Rudjer Bošković Institute, Zagreb, Croatia

Bibliography

[1] B. Armbruster et. al. "Anomaly in the time distribution of neutrinos from a pulsed beam stop source", *Physics Letters B*, **348** 19 (1995).

[2] P. Astier et. al., "Proposal: Search for the Oscillation nu-mu to nu-tau", CERN internal preprint CERN-SPSLC/91-21 SPSC/P261, March 11, 1991.

[3] Proceedings from the "Neutrino 96" Conference, Helsinki, Finland, June 13-20, 1996.

[4] V. Barger et al., "Remarks on the KARMEN Anomaly", *Physics Letters B*, **352** 365 (1995).

[5] J. Govaerts et al., "Laboratory Constraints on a 33.9 MeV/c^2 Isosingliet Neutrino: Status and Perspectives", Preprint from l'Institut de Physique Nucléaire, Université catholique de Louvain, B-1348 Louvain-la-Neuve, Belgium, UCL-IPN-96-P04, August, 1996.

[6] M. Guzzo et al., "Neutrino mixing effects on the τ-neutrino mass limit", *Physical Review D*, **53**, 2851 (1996).

[7] V. Barger et al., Erratum to "Remarks on the KARMEN Anomaly", *Physics Letters B*, **356** 617 (1995).

[8] J. Peltoniemi, "Sterile neutrinos as a solution to all neutrino anomalies", Preprint HEP-PH-9506228, June 5, 1995.

[9] D. Choudhury and S. Sarkar, *Physics Letters B* **374**, 87 (1996).

[10] ALEPH Collaboration, D. Buskulic et. al., Physics Letters B **349**, 585 (1995).

[11] M. Doran ed. *Experiments at CERN 1995*, CERN internal

[12] M. Barth and C. Ruiz *CERN Telephone Directory 1996*, CERN internal publication, central pullout map, January 1996.

[13] L. Casagrande et. al., "The Alignment of the CERN West Area Neutrino Facility", CERN internal publication CERN 96-06, Geneva, 1996.

[14] E. Tsesmelis, personal communication and Neutrino Beam Study Group Minutes.

[15] G. Acquistapace et. al. , "The West Area Neutrino Facility for Chorus and NOMAD experiments (94-97) operation", CERN internal publication CERN ECP/95-14, July 31, 1995.

[16] C. Brome et. al., "Nomad by Numbers", NOMAD internal note 72, November 18, 1994.

[17] J. Altegoer et. al., "Instrumenting the Front 'I's of NOMAD", NOMAD internal note 95-011, March 7, 1995.

[18] J. D. Jackson, *Classical Electrodynamics*, John Wiley and Sons, New York, 2nd Edition, pp. 685, 699 (1975).

[19] Burkhard Schmidt, unpublished contribution to NOMAD detector paper. publication, 1996.

[20] L. Camilleri, NOMAD internal note 10, September 25, 1992.

[21] G. Ballocchi, L. Camilleri, A. Rubbia, and D. Steele, NOMAD internal note 34, September 15, 1993.

[22] The Institute of Electrical and Electronic Engineers (IEEE) Inc., *IEEE FASTBUS Modular High-Speed Data Acquisition and Control System*, John Wiley and Sons, New York, 1986.

[23] G. Ingelman, LEPTO version 6.1 — The Lund Monte Carlo for Deep-Inelastic Lepton-Nucleon Scattering, (published in proceedings from) *Physics at Hera*, Hamburg, Germany, October 1991.

[24] A. Rubbia, *NOMAD Event Generator Offline Manual*, Nomad internal note 17 (+errata), December 20, 1994.

[25] J. Altegoer, T. Dignan, A. Geiser, D. Gibin, J.P. Meyer, P. Nédélec, M. Steininger, S. Valuev, K. Varvell, and T. Weiße, *NOMAD Géant Offline Manual version 5.11*, NOMAD internal publication, July 3, 1996.

[26] M. Goosens et al., *GÉANT — Detector Description and Simulation Tool*, CERN Program Library Long Writeup W5013 (Revised), CERN, Geneva, Switzerland, March, 1995.

[27] R. Bilger et al., "Search for the Hypothetical $\pi \to \mu x$ Decay", *Physics Letters B* **363**, (1995) 41.

[28] M. Daum et al, "Search for a neutral particle of mass 33.9 MeV in pion decay", *Physics Letters B*, **361** (1995) 179.

[29] D. Bryman and T Numao, "Search for Massive neutrinos in $\pi^+ \to \mu^+ \nu$ decay", *Physical Review D* **53**, 1 (1996), 558.